SANDIA REPORT
SAND2017-8848
Unlimited Release
Printed August, 2017

Nonlinear to Linear Elastic Code Coupling in 2-D Axisymmetric Media

Leiph A. Preston

Prepared by
Sandia National Laboratories
Albuquerque, New Mexico 87185 and Livermore, California 94550

Sandia National Laboratories is a multimission laboratory managed and operated by National Technology and Engineering Solutions of Sandia, LLC, a wholly owned subsidiary of Honeywell International, Inc., for the U.S. Department of Energy's National Nuclear Security Administration under contract DE-NA0003525.

Sandia National Laboratories

Issued by Sandia National Laboratories, operated for the United States Department of Energy by National Technology and Engineering Solutions of Sandia, LLC.

Available to DOE and DOE contractors from

U.S. Department of Energy
Office of Scientific and Technical Information
P.O. Box 62
Oak Ridge, TN 37831

Telephone: (865) 576-8401
Facsimile: (865) 576-5728
E-Mail: reports@osti.gov
Online ordering: http://www.osti.gov/scitech

Available to the public from

U.S. Department of Commerce
National Technical Information Service
5301 Shawnee Rd
Alexandria, VA 22312

Telephone: (800) 553-6847
Facsimile: (703) 605-6900
E-Mail: orders@ntis.gov
Online order: https://classic.ntis.gov/help/order-methods/

SAND2017-8848
Printed August, 2017
Unlimited Release

Nonlinear to Linear Elastic Code Coupling in 2-D Axisymmetric Media

Leiph Preston
Geophysics Department
Sandia National Laboratories
P. O. Box 5800
Albuquerque, New Mexico 87185-MS0750

Abstract

Explosions within the earth nonlinearly deform the local media, but at typical seismological observation distances, the seismic waves can be considered linear. Although nonlinear algorithms can simulate explosions in the very near field well, these codes are computationally expensive and inaccurate at propagating these signals to great distances. A linearized wave propagation code, coupled to a nonlinear code, provides an efficient mechanism to both accurately simulate the explosion itself and to propagate these signals to distant receivers. To this end we have coupled Sandia's nonlinear simulation algorithm CTH to a linearized elastic wave propagation code for 2-D axisymmetric media (axiElasti) by passing information from the nonlinear to the linear code via time-varying boundary conditions. In this report, we first develop the 2-D axisymmetric elastic wave equations in cylindrical coordinates. Next we show how we design the time-varying boundary conditions passing information from CTH to axiElasti, and finally we demonstrate the coupling code via a simple study of the elastic radius.

ACKNOWLEDGMENTS

The author would like to acknowledge Bill Hilbun for his help in this project. He provided the CTH output tracers and images for Figure 6 used in this report and gladly accommodated my requests for changes to models.

TABLE OF CONTENTS

1. Introduction 9

2. AxiElasti: 2-D AxiSymmetric Linear Elastic Wave Propagation 11
   - 2.1. Elastic Wave Equations in Cylindrical Coordinates 11
     - 2.1.1. Near the Symmetry Axis 14
     - 2.1.2. Sources 14
   - 2.2. Finite-Difference Implementation 16
     - 2.2.1. Finite-Difference Scheme 16
     - 2.2.2. Finite-Difference Equations 16
     - 2.2.3. Near the Symmetry Axis 21
     - 2.2.4. Sources 22
     - 2.2.5. Receivers 23
     - 2.2.6. Absorbing Boundary Conditions 24
     - 2.2.7. Choice of Cell Size 26
     - 2.2.8. Stability 26

3. Nonlinear to Linear Code Coupling 29
   - 3.1. Time-Varying Boundary Condition Implementation 29
   - 3.2. CTH Tracers 30
   - 3.3. Boundary Shape and Placement 30
   - 3.4. Verification of the axiElasti Implementation 31

4. Investigation of the Elastic Radius 33
   - 4.1. Modeling Setup 33
   - 4.2. Determination of Ambient Wave Speed 33
   - 4.3. Elastic Radius and Effect of Coupling Distance 36
   - 4.4. Discussion 41

5. Conclusions and Future Work 43

References 45

FIGURES

Figure 1: Finite difference scheme 16
Figure 2: Pressure waveform comparison 3-D to axiElasti 23
Figure 3: Velocity waveform comparison 3-D to axiElasti 24
Figure 4: Time-varying boundary condition scheme 29
Figure 5: Validation of time-varying boundary condition 31
Figure 6: CTH pressure and radial velocity snapshots 34
Figure 7: Raw CTH pressure tracers along radial-axis 35
Figure 8: Shock wave speed versus distance 36
Figure 9: axiElasti pressure traces as a function of coupling distance for soft granite 37
Figure 10: axiElasti pressure traces as a function of coupling distance for salt 38
Figure 11: axiElasti pressure traces as a function of coupling distance for basalt 38
Figure 12: axiElasti pressure traces as a function of coupling distance for quartz 39
Figure 13: axiElasti pressure traces as a function of coupling distance for strong granite 39

Figure 14: Amplitude ratios as a function of coupling distance 40
Figure 15: Cross-correlation coefficients as a function of coupling distance 40

TABLES

Table 1: Ambient wave speeds and densities 37
Table 2: Elastic radii for different materials and methods 41

NOMENCLATURE

Abbreviation	Definition
FD	Finite-difference
TVBC	Time-varying boundary conditions
PML	Perfectly matched layer
CPML	Convolutional perfectly matched layer
1-D	One-dimensional
2-D	Two-dimensional
3-D	Three-dimensional

1. INTRODUCTION

Explosions within the solid earth nonlinearly deform the local materials by possibly melting, crushing, breaking, and plastically deforming rocks. These nonlinear processes, by definition, must be accounted for through nonlinear equations that describe nonlinear stress-strain relationships, phase changes, material strength models, etc., and are not amenable to linear elastic wave propagation algorithms. Sandia has been developing such a nonlinear solver called CTH.

CTH is a large-deformation, strong-shock physics, massively-parallel code that can simulate shock through multiple materials in 1-D, 2-D (cartesian or cylindrical), or 3-D (Schmitt et al., 2016). It has been used to model shocks from meteorite impacts to explosions and is continuously being augmented and improved by Sandia. Material compressive and tensile strength parameters are incorporated by several possible equation of state models.

Although nonlinear algorithms, such as CTH, are able to simulate explosions in the very near field well, they are computationally expensive, require knowledge about many properties of materials that are poorly understood, especially over broad spatial regions, and become inaccurate at propagating seismic signals to great distances. Beyond a certain distance from the source, called the elastic radius, particle motions are sufficiently small that nonlinear effects become negligible and linear elastic equations can be utilized to simulate wave propagation accurately. Besides being much more computationally efficient than nonlinear algorithms, linear algorithms also require knowledge of fewer material parameters. For example, for an isotropic, elastic media, only the compressional (P) wave speed, shear (S) wave speed, and density of the material need to have reasonable approximations. These properties can be gleaned from a variety of geophysical characterization techniques that do not need access to the material directly, but can be inferred via seismic inversion techniques.

Coupling these two types of algorithms so that the near-source, nonlinear portion of the simulation domain is computed via a nonlinear algorithm, such as CTH, and, beyond the elastic radius, a linear wave propagation algorithm is used, provides optimal accuracy for the computational expense. As such, we have developed a technique based on time-varying boundary conditions where output motions from CTH are used to drive input conditions for the 2-D axisymmetric linear, elastic wave propagation code called axiElasti.

The first portion of this report will outline the derivation and implementation of the 2-D axisymmetric, cylindrical coordinate linear elastic wave equations. The second part will describe the numerical coupling between the two algorithms. The final section will demonstrate results from coupled simulation runs to explore the elastic radius in simple models.

2. AXIELASTI: 2-D AXISYMMETRIC LINEAR ELASTIC WAVE PROPAGATION

2.1. Elastic Wave Equations in Cylindrical Coordinates

The equations that govern 3-D linear wave propagation in an isotropic, elastic media can be expressed as a coupled system of first-order partial differential equations called the velocity-stress system:

$$
\begin{aligned}
\frac{\partial v_x(\mathbf{x},t)}{\partial t} &= \frac{1}{\rho(\mathbf{x})}\left(\frac{\partial \sigma_{xx}(\mathbf{x},t)}{\partial x}+\frac{\partial \sigma_{xy}(\mathbf{x},t)}{\partial y}+\frac{\partial \sigma_{xz}(\mathbf{x},t)}{\partial z}\right)\\
\frac{\partial v_y(\mathbf{x},t)}{\partial t} &= \frac{1}{\rho(\mathbf{x})}\left(\frac{\partial \sigma_{xy}(\mathbf{x},t)}{\partial x}+\frac{\partial \sigma_{yy}(\mathbf{x},t)}{\partial y}+\frac{\partial \sigma_{yz}(\mathbf{x},t)}{\partial z}\right)\\
\frac{\partial v_z(\mathbf{x},t)}{\partial t} &= \frac{1}{\rho(\mathbf{x})}\left(\frac{\partial \sigma_{xz}(\mathbf{x},t)}{\partial x}+\frac{\partial \sigma_{yz}(\mathbf{x},t)}{\partial y}+\frac{\partial \sigma_{zz}(\mathbf{x},t)}{\partial z}\right)\\
\frac{\partial \sigma_{xx}(\mathbf{x},t)}{\partial t} &= \lambda(\mathbf{x})\left(\frac{\partial v_x(\mathbf{x},t)}{\partial x}+\frac{\partial v_y(\mathbf{x},t)}{\partial y}+\frac{\partial v_z(\mathbf{x},t)}{\partial z}\right)+2\mu(\mathbf{x})\frac{\partial v_x(\mathbf{x},t)}{\partial x}\\
\frac{\partial \sigma_{yy}(\mathbf{x},t)}{\partial t} &= \lambda(\mathbf{x})\left(\frac{\partial v_x(\mathbf{x},t)}{\partial x}+\frac{\partial v_y(\mathbf{x},t)}{\partial y}+\frac{\partial v_z(\mathbf{x},t)}{\partial z}\right)+2\mu(\mathbf{x})\frac{\partial v_y(\mathbf{x},t)}{\partial y}\\
\frac{\partial \sigma_{zz}(\mathbf{x},t)}{\partial t} &= \lambda(\mathbf{x})\left(\frac{\partial v_x(\mathbf{x},t)}{\partial x}+\frac{\partial v_y(\mathbf{x},t)}{\partial y}+\frac{\partial v_z(\mathbf{x},t)}{\partial z}\right)+2\mu(\mathbf{x})\frac{\partial v_z(\mathbf{x},t)}{\partial z}\\
\frac{\partial \sigma_{xy}(\mathbf{x},t)}{\partial t} &= \mu(\mathbf{x})\left(\frac{\partial v_x(\mathbf{x},t)}{\partial y}+\frac{\partial v_y(\mathbf{x},t)}{\partial x}\right)\\
\frac{\partial \sigma_{xz}(\mathbf{x},t)}{\partial t} &= \mu(\mathbf{x})\left(\frac{\partial v_x(\mathbf{x},t)}{\partial z}+\frac{\partial v_z(\mathbf{x},t)}{\partial x}\right)\\
\frac{\partial \sigma_{yz}(\mathbf{x},t)}{\partial t} &= \mu(\mathbf{x})\left(\frac{\partial v_y(\mathbf{x},t)}{\partial z}+\frac{\partial v_z(\mathbf{x},t)}{\partial y}\right)
\end{aligned}
\tag{2.1}
$$

where v_x, v_y, and v_z are particle velocities; σ_{xx}, σ_{yy}, σ_{zz}, σ_{xz}, σ_{yz}, and σ_{xy} are stress components; ρ is density; λ and μ are the lamé and shear moduli of the medium. The velocities and stress are the dependent variables and are functions of space ($\mathbf{x}$) and time (t); density and the elastic moduli are the independent variables and are considered here to be functions of space only.

The 9 equations that make up the system given by Equation 2.1 can be written more compactly in vector notation as:

$$\frac{\partial \mathbf{v}(\mathbf{x},t)}{\partial t} = \frac{1}{\rho(\mathbf{x})}\nabla \cdot \mathbf{\Sigma}(\mathbf{x},t)$$
$$\frac{\partial \mathbf{\Sigma}(\mathbf{x},t)}{\partial t} = \mathbf{C} : \nabla \mathbf{v}(\mathbf{x},t) \tag{2.2}$$

where $\mathbf{v}$ is the velocity vector; $\mathbf{\Sigma}$ is the 3 by 3 symmetric stress tensor; and $\mathbf{C}$ is the fourth-rank elastic tensor (Dahlen and Tromp, 1998). For isotropic solids, the elastic tensor is defined by

$$C_{ijkl} = \lambda \delta_{ij}\delta_{kl} + \mu(\delta_{ik}\delta_{jl} + \delta_{il}\delta_{jk}) \tag{2.3}$$

where λ and μ are defined as before.

With Equation 2.2, we can convert the system given in cartesian coordinates in Equation 2.1 to cylindrical coordinates by using the following well-known relations (e.g., Marsden and Tromba, 1988):

$$\nabla f = \frac{\partial f}{\partial r}\hat{r} + \frac{1}{r}\frac{\partial f}{\partial \theta}\hat{\theta} + \frac{\partial f}{\partial z}\hat{z}$$
$$\nabla \cdot \mathbf{F} = \frac{1}{r}\left(\frac{\partial (rF_r)}{\partial r} + \frac{\partial F_\theta}{\partial \theta} + \frac{\partial (rF_z)}{\partial z}\right) \tag{2.4}$$

Substituting the equations from Equation 2.4 into Equation 2.2, we retrieve the linear elastic system in cylindrical coordinates:

$$\frac{\partial v_r}{\partial t} = \frac{1}{\rho}\left(\frac{\partial \sigma_{rr}}{\partial r} + \frac{1}{r}\frac{\partial \sigma_{r\theta}}{\partial \theta} + \frac{\partial \sigma_{rz}}{\partial z} + \frac{\sigma_{rr} - \sigma_{\theta\theta}}{r}\right)$$
$$\frac{\partial v_\theta}{\partial t} = \frac{1}{\rho}\left(\frac{\partial \sigma_{r\theta}}{\partial r} + \frac{1}{r}\frac{\partial \sigma_{\theta\theta}}{\partial \theta} + \frac{\partial \sigma_{\theta z}}{\partial z} + \frac{2\sigma_{r\theta}}{r}\right)$$
$$\frac{\partial v_z}{\partial t} = \frac{1}{\rho}\left(\frac{\partial \sigma_{rz}}{\partial r} + \frac{1}{r}\frac{\partial \sigma_{\theta z}}{\partial \theta} + \frac{\partial \sigma_{zz}}{\partial z} + \frac{\sigma_{rz}}{r}\right)$$
$$\frac{\partial \sigma_{rr}}{\partial t} = \lambda\left(\frac{\partial v_r}{\partial r} + \frac{v_r}{r} + \frac{1}{r}\frac{\partial v_\theta}{\partial \theta} + \frac{\partial v_z}{\partial z}\right) + 2\mu\frac{\partial v_r}{\partial r}$$
$$\frac{\partial \sigma_{\theta\theta}}{\partial t} = \lambda\left(\frac{\partial v_r}{\partial r} + \frac{v_r}{r} + \frac{1}{r}\frac{\partial v_\theta}{\partial \theta} + \frac{\partial v_z}{\partial z}\right) + 2\mu\left(\frac{v_r}{r} + \frac{1}{r}\frac{\partial v_\theta}{\partial \theta}\right) \tag{2.5}$$
$$\frac{\partial \sigma_{zz}}{\partial t} = \lambda\left(\frac{\partial v_r}{\partial r} + \frac{v_r}{r} + \frac{1}{r}\frac{\partial v_\theta}{\partial \theta} + \frac{\partial v_z}{\partial z}\right) + 2\mu\frac{\partial v_z}{\partial z}$$
$$\frac{\partial \sigma_{r\theta}}{\partial t} = \mu\left(\frac{\partial v_\theta}{\partial r} - \frac{v_\theta}{r} + \frac{1}{r}\frac{\partial v_r}{\partial \theta}\right)$$
$$\frac{\partial \sigma_{\theta z}}{\partial t} = \mu\left(\frac{1}{r}\frac{\partial v_z}{\partial \theta} + \frac{\partial v_\theta}{\partial z}\right)$$

$$\frac{\partial \sigma_{rz}}{\partial t} = \mu \left(\frac{\partial v_r}{\partial z} + \frac{\partial v_z}{\partial r} \right)$$

where v_r, v_θ, and v_z are velocity components; σ_{rr}, $\sigma_{\theta\theta}$, σ_{zz}, σ_{rz}, $\sigma_{r\theta}$, and $\sigma_{\theta z}$ are the stress components in cylindrical coordinates.

Simplifying to 2-D axisymmetry is equivalent to setting $\frac{\partial}{\partial \theta} = 0$. Making this substitution, one obtains the 2-D axisymmetric system of linear elastic equations:

$$\begin{aligned}
\frac{\partial v_r}{\partial t} &= \frac{1}{\rho} \left(\frac{\partial \sigma_{rr}}{\partial r} + \frac{\partial \sigma_{rz}}{\partial z} + \frac{\sigma_{rr} - \sigma_{\theta\theta}}{r} \right) \\
\frac{\partial v_\theta}{\partial t} &= \frac{1}{\rho} \left(\frac{\partial \sigma_{r\theta}}{\partial r} + \frac{\partial \sigma_{\theta z}}{\partial z} + \frac{2\sigma_{r\theta}}{r} \right) \\
\frac{\partial v_z}{\partial t} &= \frac{1}{\rho} \left(\frac{\partial \sigma_{rz}}{\partial r} + \frac{\partial \sigma_{zz}}{\partial z} + \frac{\sigma_{rz}}{r} \right) \\
\frac{\partial \sigma_{rr}}{\partial t} &= \lambda \left(\frac{\partial v_r}{\partial r} + \frac{v_r}{r} + \frac{\partial v_z}{\partial z} \right) + 2\mu \frac{\partial v_r}{\partial r} \\
\frac{\partial \sigma_{\theta\theta}}{\partial t} &= \lambda \left(\frac{\partial v_r}{\partial r} + \frac{v_r}{r} + \frac{\partial v_z}{\partial z} \right) + 2\mu \frac{v_r}{r} \\
\frac{\partial \sigma_{zz}}{\partial t} &= \lambda \left(\frac{\partial v_r}{\partial r} + \frac{v_r}{r} + \frac{\partial v_z}{\partial z} \right) + 2\mu \frac{\partial v_z}{\partial z} \\
\frac{\partial \sigma_{r\theta}}{\partial t} &= \mu \left(\frac{\partial v_\theta}{\partial r} - \frac{v_\theta}{r} \right) \\
\frac{\partial \sigma_{\theta z}}{\partial t} &= \mu \frac{\partial v_\theta}{\partial z} \\
\frac{\partial \sigma_{rz}}{\partial t} &= \mu \left(\frac{\partial v_r}{\partial z} + \frac{\partial v_z}{\partial r} \right)
\end{aligned} \tag{2.6}$$

For this version of axiElasti, we are going to further assume that azimuthal motion is zero, i.e., $v_\theta = 0$. Making this substitution, one obtains:

$$\begin{aligned}
\frac{\partial v_r}{\partial t} &= \frac{1}{\rho} \left(\frac{\partial \sigma_{rr}}{\partial r} + \frac{\partial \sigma_{rz}}{\partial z} + \frac{\sigma_{rr} - \sigma_{\theta\theta}}{r} \right) \\
\frac{\partial v_\theta}{\partial t} &= 0 \\
\frac{\partial v_z}{\partial t} &= \frac{1}{\rho} \left(\frac{\partial \sigma_{rz}}{\partial r} + \frac{\partial \sigma_{zz}}{\partial z} + \frac{\sigma_{rz}}{r} \right)
\end{aligned}$$

$$
\begin{aligned}
\frac{\partial \sigma_{rr}}{\partial t} &= \lambda \left(\frac{\partial v_r}{\partial r} + \frac{v_r}{r} + \frac{\partial v_z}{\partial z} \right) + 2\mu \frac{\partial v_r}{\partial r} \\
\frac{\partial \sigma_{\theta\theta}}{\partial t} &= \lambda \left(\frac{\partial v_r}{\partial r} + \frac{v_r}{r} + \frac{\partial v_z}{\partial z} \right) + 2\mu \frac{v_r}{r} \\
\frac{\partial \sigma_{zz}}{\partial t} &= \lambda \left(\frac{\partial v_r}{\partial r} + \frac{v_r}{r} + \frac{\partial v_z}{\partial z} \right) + 2\mu \frac{\partial v_z}{\partial z} \\
\frac{\partial \sigma_{r\theta}}{\partial t} &= 0 \\
\frac{\partial \sigma_{\theta z}}{\partial t} &= 0 \\
\frac{\partial \sigma_{rz}}{\partial t} &= \mu \left(\frac{\partial v_r}{\partial z} + \frac{\partial v_z}{\partial r} \right)
\end{aligned}
\tag{2.7}
$$

The assumptions made to derive Equations 2.6 and 2.7 eliminate 3 equations completely and simplify the remaining equations. Equation 2.7 constitutes the system of equations that form the basis for axiElasti's computations.

2.1.1. Near the Symmetry Axis

An investigation of Equations 2.7, reveals that there are several terms that behave as $1/r$. Near the symmetry axis, i.e., $r = 0$, these terms become singularities. In the section on implementation, we will describe the methods taken to avoid these singularities.

2.1.2. Sources

2.1.2.1. Body Force Sources

Body force sources (force per unit volume) are the inhomogeneous terms to the velocity equations. The appropriate component of the vector force source (F_r or F_z)is applied to the corresponding velocity update terms, i.e.,

$$
\begin{aligned}
\frac{\partial v_r}{\partial t} &= \frac{1}{\rho} \left(\frac{\partial \sigma_{rr}}{\partial r} + \frac{\partial \sigma_{rz}}{\partial z} + \frac{\sigma_{rr} - \sigma_{\theta\theta}}{r} + F_r \right) \\
\frac{\partial v_z}{\partial t} &= \frac{1}{\rho} \left(\frac{\partial \sigma_{rz}}{\partial r} + \frac{\partial \sigma_{zz}}{\partial z} + \frac{\sigma_{rz}}{r} + F_z \right)
\end{aligned}
\tag{2.8}
$$

2.1.2.2. Moment Sources

Moment sources in cylindrical coordinates simply involve a tensor coordinate transformation from 3-D cartesian to cylindrical coordinates of the symmetric seismic moment tensor. Performing this tensor rotation, one obtains the following relationships between the cylindrical coordinate moment tensor terms and those in cartesian coordinates:

$$
\begin{aligned}
M_{rr} &= M_{xx}\cos^2\theta + 2M_{xy}\sin\theta\cos\theta + M_{yy}\sin^2\theta \\
M_{\theta\theta} &= M_{xx}\sin^2\theta - 2M_{xy}\sin\theta\cos\theta + M_{yy}\cos^2\theta \\
M_{zz} &= M_{zz} \\
M_{rz} &= M_{xz}\cos\theta + M_{yz}\sin\theta \\
M_{r\theta} &= -M_{xx}\sin\theta\cos\theta + M_{xy}\left(-\sin^2\theta + \cos^2\theta\right) + M_{yy}\sin\theta\cos\theta \\
M_{\theta z} &= -M_{xz}\sin\theta + M_{yz}\cos\theta
\end{aligned} \tag{2.9}
$$

where $M_{xx}, M_{yy}, M_{zz}, M_{xy}, M_{xz}$, and M_{yz} comprise the moment tensor components in cartesian coordinates; $M_{rr}, M_{\theta\theta}, M_{zz}, M_{rz}, M_{\theta z}$, and $M_{r\theta}$ are the corresponding cylindrical coordinate components; and θ is the azimuthal angle relative to the x-axis.

For axisymmetric problems the moment tensor must be independent of azimuthal angle. This imposes some restrictions on what the cartesian components can be:

$$
\begin{aligned}
M_{xx} &= M_{yy} \\
M_{xy} &= 0 \\
M_{xz} &= M_{rz}\cos\theta \\
M_{yz} &= M_{rz}\sin\theta
\end{aligned} \tag{2.10}
$$

With these restrictions, Equations 2.9 become

$$
\begin{aligned}
M_{rr} &= M_{xx} \\
M_{\theta\theta} &= M_{xx} \\
M_{zz} &= M_{zz} \\
M_{rz} &= M_{rz} \\
M_{r\theta} &= 0 \\
M_{\theta z} &= 0
\end{aligned} \tag{2.11}
$$

which indicates that there are only 3 independent components in the axisymmetric cylindrical system.

The time derivative of the moment tensor terms are added to its corresponding stress component

$$
\begin{aligned}
\frac{\partial\sigma_{rr}}{\partial t} &= \lambda\left(\frac{\partial v_r}{\partial r} + \frac{v_r}{r} + \frac{\partial v_z}{\partial z}\right) + 2\mu\frac{\partial v_r}{\partial r} + \frac{\partial M_{rr}}{\partial t} \\
\frac{\partial\sigma_{\theta\theta}}{\partial t} &= \lambda\left(\frac{\partial v_r}{\partial r} + \frac{v_r}{r} + \frac{\partial v_z}{\partial z}\right) + 2\mu\frac{v_r}{r} + \frac{\partial M_{\theta\theta}}{\partial t}
\end{aligned} \tag{2.12}
$$

$$\frac{\partial \sigma_{zz}}{\partial t} = \lambda \left(\frac{\partial v_r}{\partial r} + \frac{v_r}{r} + \frac{\partial v_z}{\partial z} \right) + 2\mu \frac{\partial v_z}{\partial z} + \frac{\partial M_{zz}}{\partial t}$$

$$\frac{\partial \sigma_{rz}}{\partial t} = \mu \left(\frac{\partial v_r}{\partial z} + \frac{\partial v_z}{\partial r} \right) + \frac{\partial M_{rz}}{\partial t}$$

An isotropic moment tensor represents an explosion (or implosion) source. In this case, $M_{rr} = M_{\theta\theta} = M_{zz}$ and $M_{rz} = 0$.

2.2. Finite-Difference Implementation

2.2.1. Finite-Difference Scheme

In order to discretize the equations in Equation 2.7, we utilize a standard staggered grid. In this scheme the compressive stresses, σ_{rr}, $\sigma_{\theta\theta}$, and σ_{zz}, reside on the corners of cells, the shear stress, σ_{rz}, in the center of a cell, the radial velocity, v_r, at the center of the radial edges of the cell, and the vertical velocity, v_z, at the center of the vertical edges of the cell (Figure 1). The medium parameters, ρ, λ, and μ, are coincident with the compressive stresses. The time discretization is also staggered, with all stresses updating on integer time steps and velocities updating at half-integer time steps. Staggering of the space and time variables allows compact, centered finite-difference (FD) operators to be used. The equations are discretized with fourth order accurate spatial operators and second order temporal accuracy using standard Taylor series coefficients.

2.2.2. Finite-Difference Equations

The following equations give the finite-difference formulae corresponding to Equations 2.7. In these equations, i, k, and l, are the radial, vertical, and temporal

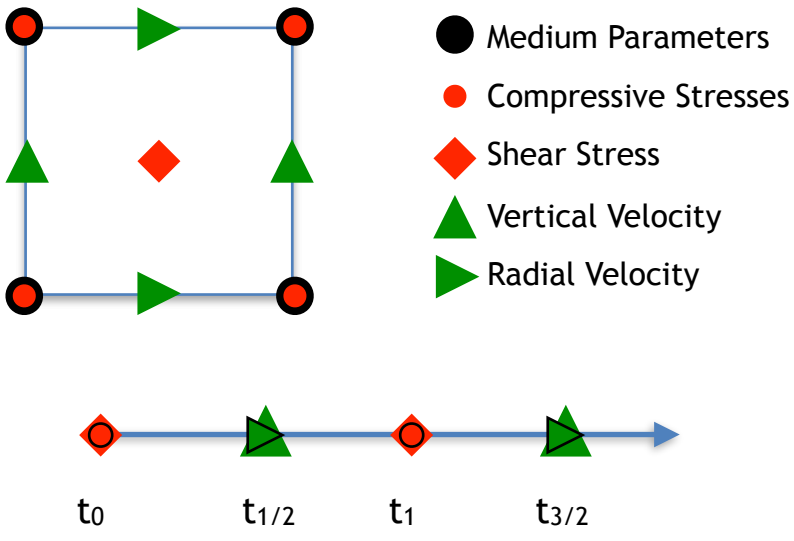

Figure 1: Unit cell (top) and time axis (bottom) for the staggered finite-difference scheme.

index numbers, respectively; d_t is the time step. The finite-difference coefficients are defined as

$$
\begin{aligned}
c_r^0 &= \frac{9}{8}\frac{1}{h_r} \\
c_r^1 &= -\frac{1}{24}\frac{1}{h_r} \\
c_z^0 &= \frac{9}{8}\frac{1}{h_z} \\
c_z^1 &= -\frac{1}{24}\frac{1}{h_z} \\
d_r^0 &= \frac{9}{16} \\
d_r^1 &= -\frac{1}{16}
\end{aligned}
\tag{2.13}
$$

where h_r and h_z are the radial and horizontal grid spacing, respectively.

Note that since density is provided on the compressional nodes, it must be interpolated onto the radial and vertical velocity node points using second order interpolation. The compressive stress updating equations do not require any interpolation of medium parameters. However, the shear stress updating equations require interpolation of the shear modulus. This is accomplished via harmonic averaging of the surrounding four shear moduli given on the corners to the central shear stress node location (Moczo et al., 2002):

$$
\mu_{i+1/2,k+1/2} = \frac{4}{\frac{1}{\mu_{i,k}} + \frac{1}{\mu_{i+1,k}} + \frac{1}{\mu_{i,k+1}} + \frac{1}{\mu_{i+1,k+1}}} \tag{2.14}
$$

2.2.2.1. Radial Velocity

$$
\begin{aligned}
v_r\left(r_{i+1/2}, z_k, t_{l+1/2}\right) &= v_r\left(r_{i+1/2}, z_k, t_{l-1/2}\right) \\
&+\frac{d_t}{\frac{1}{2}\left(\rho_{i,k}+\rho_{i+1,k}\right)}\left[c_r^{(0)}\left[\sigma_{rr}\left(r_{i+1}, z_k, t_l\right)-\sigma_{rr}\left(r_i, z_k, t_l\right)\right]\right. \\
&\quad +c_r^{(1)}\left[\sigma_{rr}\left(r_{i+2}, z_k, t_l\right)-\sigma_{rr}\left(r_{i-1}, z_k, t_l\right)\right] \\
&\quad +c_z^{(0)}\left[\sigma_{rz}\left(r_{i+1/2}, z_{k+1/2}, t_l\right)-\sigma_{rz}\left(r_{i+1/2}, z_{k-1/2}, t_l\right)\right] \\
&\quad +c_z^{(1)}\left[\sigma_{rz}\left(r_{i+1/2}, z_{k+3/2}, t_l\right)-\sigma_{rz}\left(r_{i+1/2}, z_{k-3/2}, t_l\right)\right] \\
&\quad +\frac{1}{r_{i+1/2}}\left[d_r^{(0)}\left[\sigma_{rr}\left(r_i, z_k, t_l\right)+\sigma_{rr}\left(r_{i+1}, z_k, t_l\right)\right]\right. \\
&\qquad +d_r^{(1)}\left[\sigma_{rr}\left(r_{i-1}, z_k, t_l\right)+\sigma_{rr}\left(r_{i+2}, z_k, t_l\right)\right] \\
&\qquad -d_r^{(0)}\left[\sigma_{\theta\theta}\left(r_i, z_k, t_l\right)+\sigma_{\theta\theta}\left(r_{i+1}, z_k, t_l\right)\right] \\
&\qquad \left.\left.-d_r^{(1)}\left[\sigma_{\theta\theta}\left(r_{i-1}, z_k, t_l\right)+\sigma_{\theta\theta}\left(r_{i+2}, z_k, t_l\right)\right]\right]\right]
\end{aligned}
\tag{2.15}
$$

2.2.2.2. Vertical Velocity

$$
\begin{aligned}
v_z\left(r_i, z_{k+1/2}, t_{l+1/2}\right) &= v_z\left(r_i, z_{k+1/2}, t_{l-1/2}\right) \\
&+\frac{d_t}{\frac{1}{2}\left(\rho_{i,k}+\rho_{i,k+1}\right)}\left[c_r^{(0)}\left[\sigma_{rz}\left(r_{i+1/2}, z_{k+1/2}, t_l\right)-\sigma_{rz}\left(r_{i-1/2}, z_{k+1/2}, t_l\right)\right]\right. \\
&\quad +c_r^{(1)}\left[\sigma_{rz}\left(r_{i+3/2}, z_{k+1/2}, t_l\right)-\sigma_{rz}\left(r_{i-3/2}, z_{k+1/2}, t_l\right)\right] \\
&\quad +c_z^{(0)}\left[\sigma_{zz}\left(r_i, z_{k+1}, t_l\right)-\sigma_{zz}\left(r_i, z_k, t_l\right)\right] \\
&\quad +c_z^{(1)}\left[\sigma_{zz}\left(r_i, z_{k+2}, t_l\right)-\sigma_{zz}\left(r_i, z_{k-1}, t_l\right)\right] \\
&\quad +\frac{1}{r_i}\left[d_r^{(0)}\left[\sigma_{rz}\left(r_{i+1/2}, z_{k+1/2}, t_l\right)+\sigma_{rz}\left(r_{i-1/2}, z_{k+1/2}, t_l\right)\right]\right. \\
&\qquad \left.\left.+d_r^{(1)}\left[\sigma_{rz}\left(r_{i+3/2}, z_{k+1/2}, t_l\right)+\sigma_{rz}\left(r_{i-3/2}, z_{k+1/2}, t_l\right)\right]\right]\right]
\end{aligned}
\tag{2.16}
$$

2.2.2.3. Radial Compressive Stress

$$
\begin{aligned}
&\sigma_{rr}\left(r_i, z_k, t_{l+1}\right) = \sigma_{rr}\left(r_i, z_k, t_l\right) \\
&\quad +\lambda_{i,k} d_t \left[c_r^{(0)} \left[v_r\left(r_{i+1/2}, z_k, t_{l+1/2}\right) - v_r\left(r_{i-1/2}, z_k, t_{l+1/2}\right) \right] \right. \\
&\qquad +c_r^{(1)} \left[v_r\left(r_{i+3/2}, z_k, t_{l+1/2}\right) - v_r\left(r_{i-3/2}, z_k, t_{l+1/2}\right) \right] \\
&\qquad +c_z^{(0)} \left[v_z\left(r_i, z_{k+1/2}, t_{l+1/2}\right) - v_z\left(r_i, z_{k-1/2}, t_{l+1/2}\right) \right] \\
&\qquad +c_z^{(1)} \left[v_z\left(r_i, z_{k+3/2}, t_{l+1/2}\right) - v_z\left(r_i, z_{k-3/2}, t_{l+1/2}\right) \right] \\
&\qquad +\frac{1}{r_i} \left[d_r^{(0)} \left[v_r\left(r_{i+1/2}, z_k, t_{l+1/2}\right) + v_r\left(r_{i-1/2}, z_k, t_{l+1/2}\right) \right] \right. \\
&\qquad\quad \left. \left. +d_r^{(1)} \left[v_r\left(r_{i+3/2}, z_k, t_{l+1/2}\right) + v_r\left(r_{i-3/2}, z_k, t_{l+1/2}\right) \right] \right] \right] \\
&\quad +2\mu_{i,k} d_t \left[c_r^{(0)} \left[v_r\left(r_{i+1/2}, z_k, t_{l+1/2}\right) - v_r\left(r_{i-1/2}, z_k, t_{l+1/2}\right) \right] \right. \\
&\qquad \left. +c_r^{(1)} \left[v_r\left(r_{i+3/2}, z_k, t_{l+1/2}\right) - v_r\left(r_{i-3/2}, z_k, t_{l+1/2}\right) \right] \right]
\end{aligned}
\tag{2.17}
$$

2.2.2.4. Azimuthal Compressive Stress

$$
\begin{aligned}
&\sigma_{\theta\theta}\left(r_i, z_k, t_{l+1}\right) = \sigma_{\theta\theta}\left(r_i, z_k, t_l\right) \\
&\quad +\lambda_{i,k} d_t \left[c_r^{(0)} \left[v_r\left(r_{i+1/2}, z_k, t_{l+1/2}\right) - v_r\left(r_{i-1/2}, z_k, t_{l+1/2}\right) \right] \right. \\
&\qquad +c_r^{(1)} \left[v_r\left(r_{i+3/2}, z_k, t_{l+1/2}\right) - v_r\left(r_{i-3/2}, z_k, t_{l+1/2}\right) \right] \\
&\qquad +c_z^{(0)} \left[v_z\left(r_i, z_{k+1/2}, t_{l+1/2}\right) - v_z\left(r_i, z_{k-1/2}, t_{l+1/2}\right) \right] \\
&\qquad +c_z^{(1)} \left[v_z\left(r_i, z_{k+3/2}, t_{l+1/2}\right) - v_z\left(r_i, z_{k-3/2}, t_{l+1/2}\right) \right] \\
&\qquad +\frac{1}{r_i} \left[d_r^{(0)} \left[v_r\left(r_{i+1/2}, z_k, t_{l+1/2}\right) + v_r\left(r_{i-1/2}, z_k, t_{l+1/2}\right) \right] \right. \\
&\qquad\quad \left. \left. +d_r^{(1)} \left[v_r\left(r_{i+3/2}, z_k, t_{l+1/2}\right) + v_r\left(r_{i-3/2}, z_k, t_{l+1/2}\right) \right] \right] \right] \\
&\quad +2\mu_{i,k} d_t \left[\frac{1}{r_i} \left[d_r^{(0)} \left[v_r\left(r_{i+1/2}, z_k, t_{l+1/2}\right) + v_r\left(r_{i-1/2}, z_k, t_{l+1/2}\right) \right] \right. \right. \\
&\qquad\quad \left. \left. +d_r^{(1)} \left[v_r\left(r_{i+3/2}, z_k, t_{l+1/2}\right) + v_r\left(r_{i-3/2}, z_k, t_{l+1/2}\right) \right] \right] \right]
\end{aligned}
\tag{2.18}
$$

2.2.2.5. Vertical Compressive Stress

$$
\begin{aligned}
&\sigma_{zz}\left(r_i, z_k, t_{l+1}\right) = \sigma_{zz}\left(r_i, z_k, t_l\right) \\
&\quad +\lambda_{i,k} d_t \left[c_r^{(0)} \left[v_r\left(r_{i+1/2}, z_k, t_{l+1/2}\right) - v_r\left(r_{i-1/2}, z_k, t_{l+1/2}\right) \right] \right. \\
&\qquad +c_r^{(1)} \left[v_r\left(r_{i+3/2}, z_k, t_{l+1/2}\right) - v_r\left(r_{i-3/2}, z_k, t_{l+1/2}\right) \right] \\
&\qquad +c_z^{(0)} \left[v_z\left(r_i, z_{k+1/2}, t_{l+1/2}\right) - v_z\left(r_i, z_{k-1/2}, t_{l+1/2}\right) \right] \\
&\qquad +c_z^{(1)} \left[v_z\left(r_i, z_{k+3/2}, t_{l+1/2}\right) - v_z\left(r_i, z_{k-3/2}, t_{l+1/2}\right) \right] \\
&\qquad +\frac{1}{r_i} \left[d_r^{(0)} \left[v_r\left(r_{i+1/2}, z_k, t_{l+1/2}\right) + v_r\left(r_{i-1/2}, z_k, t_{l+1/2}\right) \right] \right. \\
&\qquad\quad \left. \left. +d_r^{(1)} \left[v_r\left(r_{i+3/2}, z_k, t_{l+1/2}\right) + v_r\left(r_{i-3/2}, z_k, t_{l+1/2}\right) \right] \right] \right] \\
&\quad +2\mu_{i,k} d_t \left[c_z^{(0)} \left[v_z\left(r_i, z_{k+1/2}, t_{l+1/2}\right) - v_z\left(r_i, z_{k-1/2}, t_{l+1/2}\right) \right] \right. \\
&\qquad \left. +c_z^{(1)} \left[v_z\left(r_i, z_{k+3/2}, t_{l+1/2}\right) - v_z\left(r_i, z_{k-3/2}, t_{l+1/2}\right) \right] \right]
\end{aligned}
\tag{2.19}
$$

2.2.2.6. Radial-Vertical Shear Stress

$$
\begin{aligned}
&\sigma_{rz}\left(r_{i+1/2}, z_{k+1/2}, t_{l+1}\right) = \sigma_{rz}\left(r_{i+1/2}, z_{k+1/2}, t_l\right) \\
&\quad +\mu_{i+1/2,k+1/2} d_t \left[c_z^{(0)} \left[v_r\left(r_{i+1/2}, z_{k+1}, t_{l+1/2}\right) - v_r\left(r_{i+1/2}, z_k, t_{l+1/2}\right) \right] \right. \\
&\qquad +c_z^{(1)} \left[v_r\left(r_{i+1/2}, z_{k+2}, t_{l+1/2}\right) - v_r\left(r_{i+1/2}, z_{k-1}, t_{l+1/2}\right) \right] \\
&\qquad +c_r^{(0)} \left[v_z\left(r_{i+1}, z_{k+1/2}, t_{l+1/2}\right) - v_z\left(r_i, z_{k+1/2}, t_{l+1/2}\right) \right] \\
&\qquad \left. +c_r^{(1)} \left[v_z\left(r_{i+2}, z_{k+1/2}, t_{l+1/2}\right) - v_z\left(r_{i-1}, z_{k+1/2}, t_{l+1/2}\right) \right] \right]
\end{aligned}
\tag{2.20}
$$

2.2.3. Near the Symmetry Axis

As mentioned in Section 2.1.1, the axisymmetric equations exhibit singularities at the symmetry axis itself. Additionally, the finite-difference equations (Equations 2.15-2.20) require "reaching" over the symmetry axis when close to the symmetry axis. The 1/r term in the radial velocity equation (2.15) is a non-issue since radial velocity is never computed directly at r=0; i.e., it is staggered one-half grid node off the axis. However, the vertical velocity component and all the compressive stress components have 1/r terms and are calculated directly at r=0. Based on symmetry

arguments and the fact that the terms involving 1/r in these equations are stand-ins for the 3-D cartesian y-coordinate (assuming the x-axis would be aligned with the r-axis), at r=0,

$$\lim_{r\to 0}\frac{v_r}{r} = \frac{\partial v_r}{\partial r}$$
$$\lim_{r\to 0}\frac{\sigma_{rz}}{r} = \frac{\partial \sigma_{rz}}{\partial r} \qquad (2.21)$$

Thus, we can simply replace these 1/r terms in Equations 2.16-2.19 with those of Equation 2.21 at r=0.

The second issue involves the need to "reach" over the symmetry axis with fourth order finite-difference operators when close to the r=0 axis. Here, symmetry considerations allow us to fill in these missing values with ones that do exist within the grid.

$$v_r(-r) = -\,v_r(r)$$
$$v_z(-r) = v_z(r)$$
$$\sigma_{rr}(-r) = \sigma_{rr}(r) \qquad (2.22)$$
$$\sigma_{rz}(-r) = -\,\sigma_{rz}(r)$$

Note that neither $\sigma_{\theta\theta}$ nor σ_{zz} is needed across the symmetry axis.

By taking Equations 2.21 and 2.22 into account, Equations 2.15-2.20 can be used everywhere in the 2-D model domain. However, special, non-centered finite-difference operators could be employed near the symmetry axis to avoid "reaching" over the axis or inaccuracies due to the rapidly growing function near this axis. Several non-centered finite-difference and interpolator operators were tested when developing this algorithm. None of these proved as accurate overall as the centered operators given here. The primary issue that was found with the centered operators is that the computed traces were a factor of $\sqrt{2}$ smaller in amplitude for all components relative to an isotropic explosion in a well-tested 3-D elastic algorithm. Tests showed that this $\sqrt{2}$ factor was due to interpolator error in v_r directly next to the source. When this factor is accounted for, amplitude differences between the 3-D and 2-D axisymmetric codes are <0.1%, waveform similarity is excellent, and, for isotropic explosions, pressure, v_r, and v_z, exhibit the symmetry they should along the r- and z-directions (Figures 2 and 3).

2.2.4. Sources

Currently, all sources are required to lie on the symmetry axis. One can choose any z-coordinate for the source. The source amplitude is linearly extrapolated to the closest two surrounding nodes if the source does not lie directly on a node.

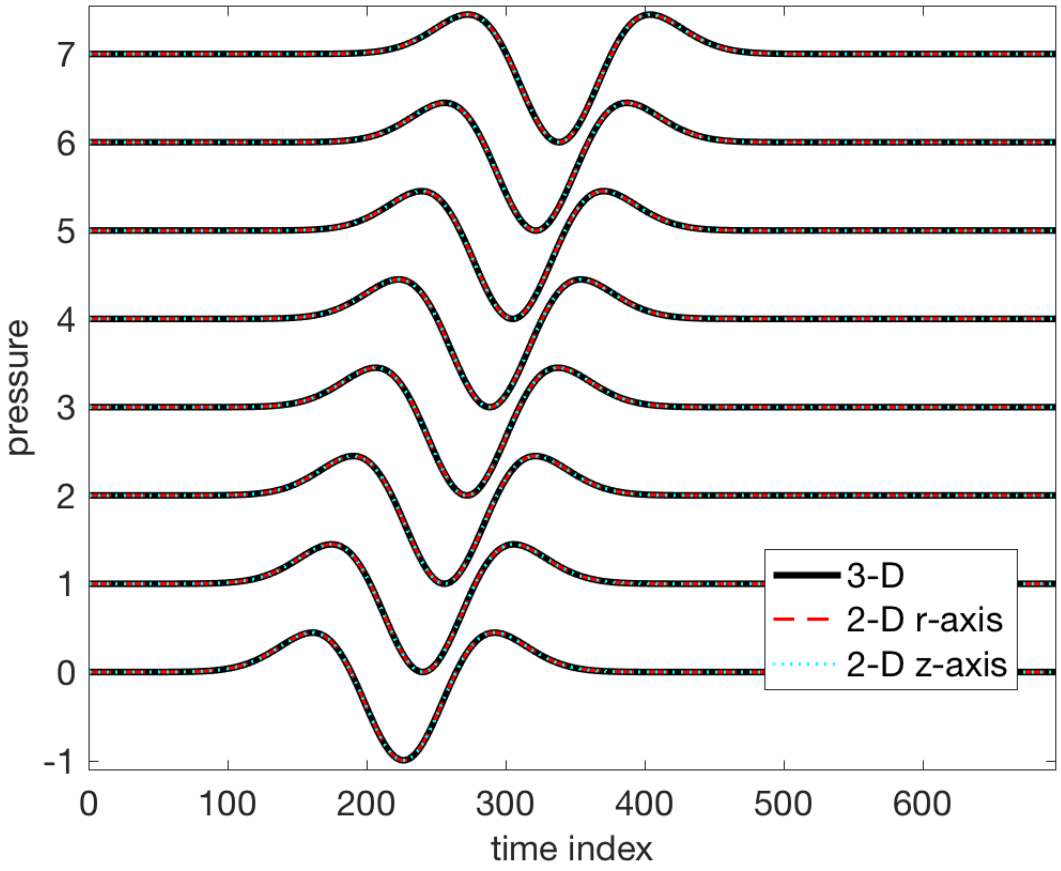

Figure 2: Comparison of pressure traces from 3-D (black) and 2-D axisymmetric algorithms using a homogeneous earth model and isotropic explosion source. For the 2-D algorithm, traces along the radial direction (red dashed) match those along the vertical direction (blue dotted).

One can also provide any arbitrary source time function for the source or specify a delta function source. In the latter case, the output traces are Greens Functions and can be convolved with any source time function to obtain results just as if that source time function had been used originally. This provides a computationally efficient mechanism to try a variety of source time functions with a single run of the algorithm. Besides being able to provide any arbitrary source time function via an input text file, there are some ready-made source time functions, such as a Gaussian, that axiElasti can generate for the user.

2.2.5. Receivers

Receivers can be placed anywhere in the domain, but they are ill advised in the absorbing boundary zone, at the source point, or directly on the symmetry axis. These restrictions are due to numerical issues that will cause the traces to be erroneous or hard to interpret. For receivers not directly located on a node, the values are bilinearly interpolated from the surrounding four nodes.

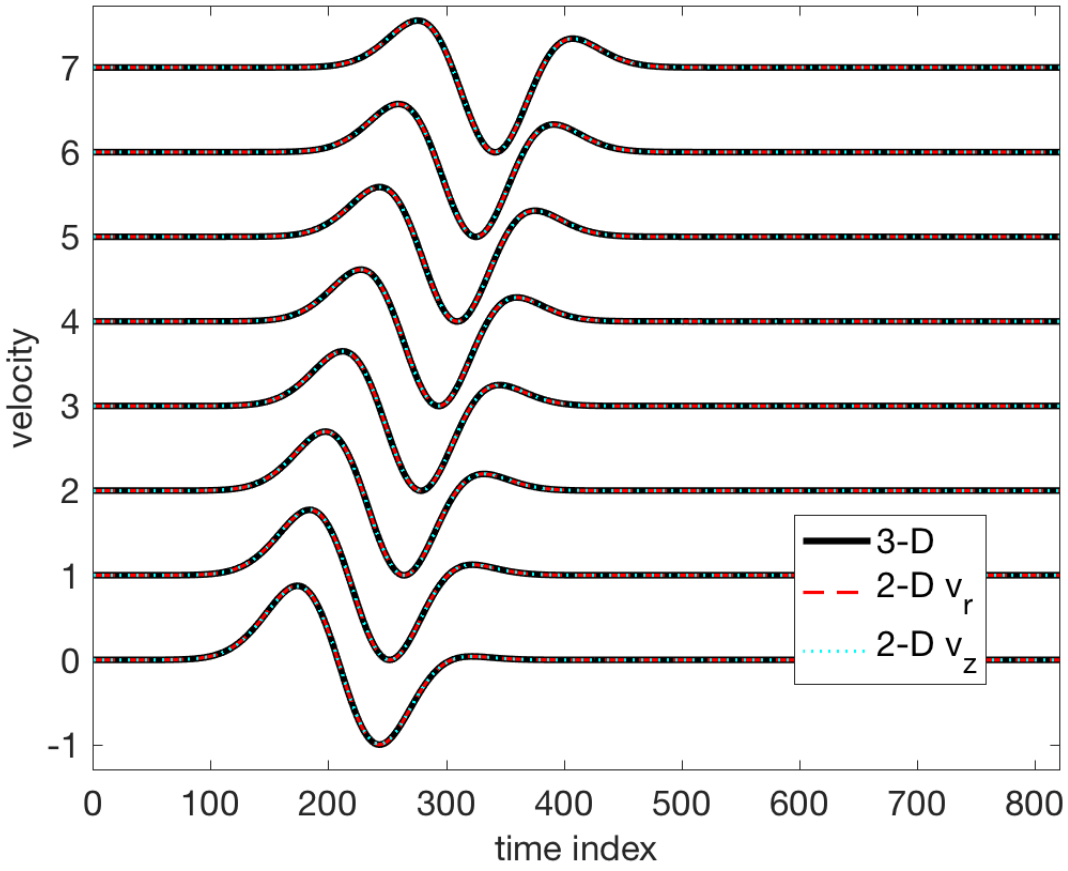

Figure 3: Comparison of velocity traces from 3-D v_x along the x direction (black) and 2-D axisymmetric algorithms using a homogeneous earth model and isotropic explosion source. For the 2-D algorithm, v_r is displayed in the radial direction and v_z along the vertical direction.

Velocity and stress component receivers are directly interpolated from their respective dependent variable. Pressure, however, is not available at every grid point and, thus, it must be computed from the compressive stress nodes via

$$p = -\frac{1}{3}\left(\sigma_{rr} + \sigma_{\theta\theta} + \sigma_{zz}\right)$$

2.2.6. Absorbing Boundary Conditions

Due to the finite size of a computational domain, absorbing boundary conditions are required to mitigate unrealistic, numerical reflections from the domain boundaries. The z boundaries (top and bottom) can utilize standard convolutional perfectly matched layers (CPML; Komatitsch and Martin, 2007) as are used in 3-D algorithms simply changed to 2-D. The maximum radial boundary, however, requires specialized treatment in an axisymmetric cylindrical coordinate case (Collino and Monk, 1998).

Within the maximum radial PML zone, the following differential equations apply

$$\rho\left(\frac{\partial v_r^*}{\partial t}+\gamma v_r^*\right)=\left(\frac{\partial \sigma_{rr}^*}{\partial r}+\frac{\partial \sigma_{rz}^*}{\partial z}+\frac{\tilde{\sigma}_{rr}-\tilde{\sigma}_{\theta\theta}}{r}\right)$$

$$\rho\left(\frac{\partial v_z^*}{\partial t}+\gamma v_z^*\right)=\left(\frac{\partial \tilde{\sigma}_{rz}}{\partial r}+\frac{\partial \sigma_{zz}^*}{\partial z}+\frac{\bar{\sigma}_{rz}}{r}\right)$$

$$\frac{\partial \sigma_{rr}^*}{\partial t}+\gamma\sigma_{rr}^*=\lambda\left(\frac{\partial v_r^*}{\partial r}+\frac{\tilde{v}_r}{r}+\frac{\partial \tilde{v}_z}{\partial z}\right)+2\mu\frac{\partial v_r^*}{\partial r}$$

$$\frac{\partial \sigma_{\theta\theta}^*}{\partial t}+\gamma\sigma_{\theta\theta}^*=\lambda\left(\frac{\partial v_r^*}{\partial r}+\frac{\tilde{v}_r}{r}+\frac{\partial \tilde{v}_z}{\partial z}\right)+2\mu\frac{\tilde{v}_r}{r} \tag{2.23}$$

$$\frac{\partial \tilde{\sigma}_{zz}}{\partial t}+\gamma\tilde{\sigma}_{zz}=\lambda\left(\frac{\partial v_r^*}{\partial r}+\frac{\tilde{v}_r}{r}+\frac{\partial \tilde{v}_z}{\partial z}\right)+2\mu\frac{\partial \tilde{v}_z}{\partial z}$$

$$\frac{\partial \sigma_{rz}}{\partial t}+\gamma\sigma_{rz}=\mu\left(\frac{\partial \tilde{v}_r}{\partial z}+\frac{\partial v_z}{\partial r}\right)$$

$$\frac{\partial v_r^*}{\partial t}=\frac{\partial v_r}{\partial t}+\bar{\gamma}v_r$$

$$\frac{\partial \sigma_{rr}^*}{\partial t}=\frac{\partial \sigma_{rr}}{\partial t}+\bar{\gamma}\sigma_{rr}$$

$$\frac{\partial \tilde{\sigma}_{rz}}{\partial t}=\frac{\partial \sigma_{rz}}{\partial t}+\bar{\gamma}\sigma_{rz}$$

$$\frac{\partial \sigma_{rz}^*}{\partial t}=\frac{\partial \tilde{\sigma}_{rz}}{\partial t}+\gamma\tilde{\sigma_{rz}}$$

$$\frac{\partial \tilde{\sigma}_{rr}}{\partial t}=\frac{\partial \sigma_{rr}}{\partial t}+\gamma\sigma_{rr}$$

$$\frac{\partial \tilde{\sigma}_{\theta\theta}}{\partial t}=\frac{\partial \sigma_{\theta\theta}}{\partial t}+\gamma\sigma_{\theta\theta}$$

$$\frac{\partial v_z^*}{\partial t}=\frac{\partial v_z}{\partial t}+\bar{\gamma}v_z$$

$$\frac{\partial \tilde{\sigma}_{zz}}{\partial t}=\frac{\partial \sigma_{zz}}{\partial t}+\bar{\gamma}\sigma_{zz}$$

$$\frac{\partial \sigma_{zz}^*}{\partial t}=\frac{\partial \tilde{\sigma}_{zz}}{\partial t}+\gamma\tilde{\sigma}_{zz}$$

$$\frac{\partial \bar{\sigma}_{rz}}{\partial t}=\frac{\partial \sigma_{rz}}{\partial t}+\gamma\sigma_{rz}$$

$$\frac{\partial \tilde{v}_r}{\partial t}=\frac{\partial v_r}{\partial t}+\gamma v_r$$

$$\frac{\partial \tilde{v}_z}{\partial t} = \frac{\partial v_z^*}{\partial t} + \gamma v_z^*$$
$$\frac{\partial \sigma_{\theta\theta}^*}{\partial t} = \frac{\partial \sigma_{\theta\theta}}{\partial t} + \bar{\gamma}\sigma_{\theta\theta}$$

This introduces 13 new variables and, correspondingly, 13 new equations. γ is the PML damping parameter. It is a function of r only and, in axiElasti, has a quadratic profile starting at zero at the interface between the PML and interior zone and ramps up to a maximum value at the flank. Finally,

$$\bar{\gamma}(r) = \int_{r_{ABC}}^{r_{max}} \gamma(s)\mathrm{d}s \tag{2.24}$$

where r_{max} is the radial flank of the domain and r_{ABC} is the radius at the start of the radial PML zone. Note that these equations reduce to those given in Equation 2.7 if γ is zero.

In the corners where a z and r PML zone overlap, the two can be used concurrently without any modifications.

2.2.7. Choice of Cell Size

The cell size, or node spacing, h, is typically the same in the vertical and radial directions, (i.e., $h = h_r = h_z$) for maximum accuracy. It determines the fidelity of the solution of the FD equations. The appropriate node spacing to use is based upon the minimum wave speed in the domain (V_{min})and the maximum frequency (f_{max})that one desires to be simulated,

$$h = G\frac{V_{min}}{f_{max}}$$

where G is a constant that is based upon the desired accuracy. Based on numerical phase and group speed curves for elastic media in Haney and Aldridge (2008), the optimal G is between 0.1 and 0.16. The best value depends on the time step and the model to a certain extent. For typical models with topography, surface waves, and other complications, experience shows that a value for G closer to 0.1 is optimal, whereas larger values can be used in simpler models.

2.2.8. Stability

2.2.8.1. Time step

Since this is an explicit leap-frog time-stepping algorithm, there exists a maximum time step for stability ($\max d_t$), called the Courant-Friedrichs-Lewy (CFL) condition. It is determined by the grid spacing and maximum seismic velocity (V_{max})via

$$\max d_t = \frac{h}{\sqrt{2}V_{max}\sum\left|c^{(i)}\right|} \tag{2.25}$$

where h is $\max(h_r, h_z)$ and the $c^{(i)}$ are the finite-difference coefficients given Section 2.2.2.

Although this is the maximum time step allowed for stability, it is not the optimal choice since smaller d_t will provide superior accuracy. Based on von Neumann analysis of the numerical wave speeds (Haney and Aldridge, 2008) versus computational runtime as a function of d_t, the optimal d_t is approximately $0.6 \max d_t$.

2.2.8.2. High Contrast Media

Strong contrasts, especially in density, from one grid point to the next can cause instabilities and/or inaccuracies in simulation results. Using the medium parameter averaging techniques discussed in Section 2.2.2 greatly improves performance, but still will produce inaccurate results in high contrast media. One solution that produces accurate and stable results uses the order-switching methodology outlined in Preston et al. (2008). In this method, the earth model is scanned prior to time-stepping and high contrast points are diagnosed. Finite-difference updating formulae only in the vicinity of these points are altered from fourth to second order accuracy; all other points remain at fourth order accuracy. By limiting the reach of the operators to second order, stability and accuracy can be maintained, while keeping the majority of the dependent variable updates at fourth order accuracy.

3. NONLINEAR TO LINEAR CODE COUPLING

One of the primary objectives of this work is to allow the coupling between a nonlinear algorithm, such as CTH, to a linear wave propagation algorithm, such as axiElasti, to permit computationally efficient and accurate signal generation in the near-field, nonlinear zone and propagation of seismic waves into the far-field, linear region. To accomplish this, we implement time-varying boundary conditions (TVBC) into axiElasti. This section details the implementation and procedures needed to perform a one-way transfer of information from a nonlinear code to a linear one. We will focus our attention on CTH and axiElasti, but many of the higher level principles would apply to any nonlinear to linear code coupling.

3.1. Time-Varying Boundary Condition Implementation

The basic principle behind time-varying boundary conditions is fairly straight forward. One simply supplies values for all dependent variables for all times at specified locations within the model domain. Equations 2.7 are not used at these locations, but the values come exclusively from an external source, namely output from CTH. Of course, the details of the implementation are what require special consideration.

In a finite-difference algorithm such as axiElasti, the spatial order of the FD operators must be honored in the boundary zone. Additionally, spatial and temporal staggering of the dependent variables must be accounted for. This requires that the zone have appropriate thickness in space, with possible interpolation of CTH output values in time and/or space. Since axiElasti is a fourth order, standard staggered grid FD algorithm, we need one and a half cells worth of information from the CTH domain in order to update dependent variables in the axiElasti domain (Figure 4). More specifically, to update compressive stresses and vertical velocities at point D in the axiElasti domain, from Equations 2.16-2.19, one needs radial velocities and *rz* shear stresses from points A and C in the CTH domain, respectively. Likewise, to update radial velocities and *rz* shear stress at point E in the axiElasti domain, one needs

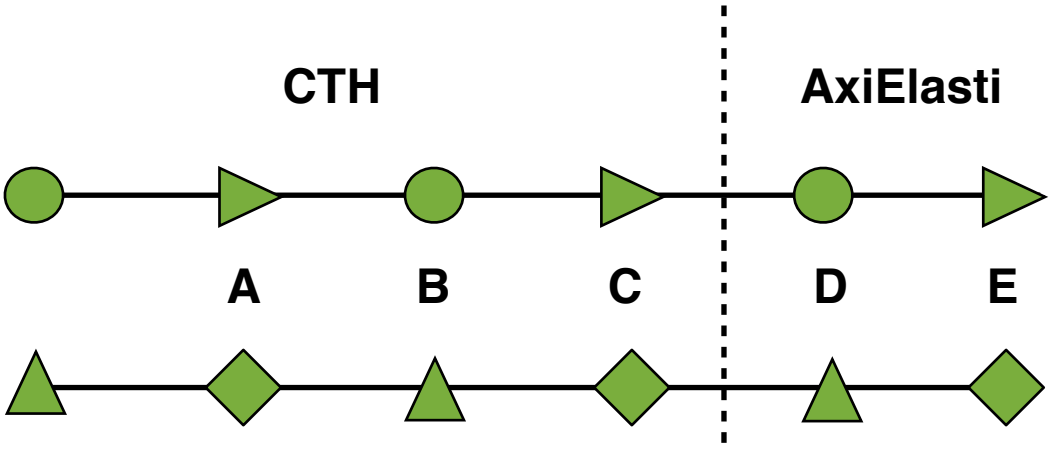

Figure 4: Required spatial distribution of velocities and stresses needed by axiElasti from the CTH domain for time varying boundary conditions.

compressive stresses and vertical velocities from points B and D, respectively. Since point D is already in the axiElasti domain, only point B is needed from the CTH domain. Thus, CTH information from points A, B, and C are required to properly perform the finite-difference computations in axiElasti.

3.2. CTH Tracers

CTH allows users to place receivers that record any of a variety of parameters or values at specified fixed locations within its domain as a function of time, called tracers. Tracers provide the information required to fill in the time-varying boundary conditions for axiElasti. As such, we need horizontal and vertical components of particle velocity, all three compressive stresses, and the *rz* stress components at the points outlined in Section 3.1. All of the needed information is available as CTH tracers in 2-D cylindrical mode except for $\sigma_{\theta\theta}$. However, this can be calculated from σ_{rr}, σ_{zz}, and v_r/r via:

$$\sigma_{\theta\theta}(t) = \frac{\lambda}{2\lambda + 2\mu}\left[\sigma_{rr}(t) + \sigma_{zz}(t)\right] + \left[\lambda + 2\mu - \frac{\lambda^2}{\lambda + \mu}\right]\int_0^t \frac{v_r(\tau)}{r}\mathrm{d}\tau \tag{3.1}$$

by rearrangement and integration of the compressive stress equations in Equation 2.7, assuming homogenous initial conditions.

Although CTH tracers can easily be chosen to lie on the FD grid with planning, the tracers must be temporally interpolated because CTH and axiElasti handle time differently. CTH runs with a variable time step to maximize accuracy and efficiency. However, axiElasti uses a fixed time step throughout. Thus, output tracers from CTH must be resampled onto the regular axiElasti time raster. Additionally, due to the nature of CTH computations, higher frequencies will be present in the CTH tracers than can be handled accurately in the FD algorithm. As such, CTH tracers are low pass filtered to the corner frequency permitted by the FD grid for accurate propagation.

One final processing step is required before the CTH tracer output data can be used as time-varying boundary conditions within axiElast. The units of CTH are cgs, whereas those of axiElasti are SI units. Velocities are converted from cm/s to m/s and stresses from dynes/cm^2 to Pa. It also must be remembered that location information given in CTH tracer files are also in cgs units, so r and z coordinates must be converted from cm to m.

3.3. Boundary Shape and Placement

The shape of the boundary can theoretically take any form as long as the principles in Section 3.1 are adhered to: axiElasti requires one and a half cell width's worth of information reaching into the boundary zone whether that be in radial or vertical direction, or both. In the current version of axiElasti only a 2-D rectangle in r and z with one edge at r=0 (a cylinder in 3-D) is implemented. CTH computes the ground response inside of this rectangle, while axiElasti will propagate waves outgoing from this rectangle. The location of the radius and minimum and maximum vertical

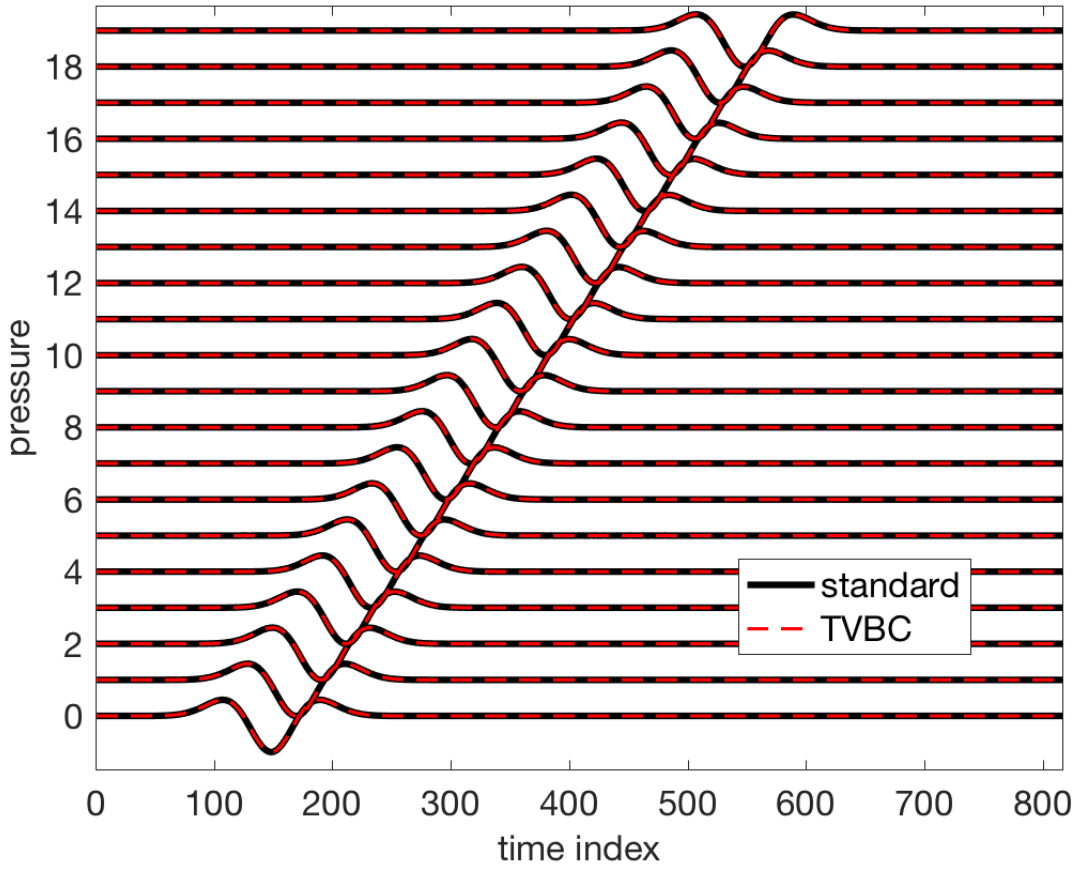

Figure 5: Comparison of pressure traces from standard axiElasti simulation (with explosive source) to axiElasti using time-varying boundary conditions (TVBC). The boundary surrounds the source and velocities and stresses were captured from the standard run and then used as input for the TVBC run.

coordinates for this rectangle are dependent on the elastic radius, where ground motions become sufficiently linear to allow accurate propagation given axiElasti's linear assumptions. The location of the elastic radius as a function of material type and the repercussions of using an incorrect elastic radius will be discussed in the following chapter.

3.4. Verification of the axiElasti Implementation

In order to test the implementation of time-varying boundary conditions in axiElasti, we first ran axiElasti with an explosion source in a homogenous medium and captured velocity and stress component traces from receivers placed along a 2-D rectangle surrounding the source. These axiElasti output traces can then be used directly as time-varying boundary conditions within a separate run of axiElasti without a source, but that uses solely time-varying boundary conditions. Waveforms from receivers outside of the time-varying boundary zone can then be compared between the standard axiElasti run with the source and the one using only time-varying boundary

conditions. Figure 5 demonstrates that the results of the two simulations are identical to machine precision, indicating that the time-varying boundary condition code within axiElasti is operating correctly. In the next chapter we will demonstrate the effectiveness of the time-varying boundary conditions when using CTH tracer output.

4. INVESTIGATION OF THE ELASTIC RADIUS

4.1. Modeling Setup

In this chapter we will show results from CTH to axiElasti code coupling numerical experiments related to the elastic radius. All of the models described are homogeneous earth models. Five different earth materials were tested: salt, basalt, strong granite, weak granite, and quartz. Salt, basalt, strong granite, and quartz material models for CTH used standard materials from the SESAME tables (Kerley and Christian-Frear, 1993) with material seslan numbers 7282, 7530, 7390, and 7386, respectively. The weak granite model (granite2 in captions) was developed by Eric Chael (personal communication) upon altering seslan 7390 to better match data collected during the Source Physics Experiment (Snelson et al., 2013).

Two-dimensional, cylindrical symmetry CTH simulations were performed in each of the five materials. In order to investigate the elastic radius, tracers were placed from roughly 2 m to 15 m from the source in the vertical and radial dimension (Figure 6), with a spacing of 14 cm to match the desired FD grid node spacing. A fully tamped 10 kg TNT explosive charge was detonated in the material on the symmetry axis. Figure 6 also shows the expansion of the initial shock wave as computed by CTH. All tracers were low-pass filtered to 2000 Hz before input into axiElasti.

4.2. Determination of Ambient Wave Speed

Following an explosion detonation, a shock wave propagates from the source with a speed faster than the speed of sound in that material. As the amplitude of the shock wave decreases as it moves farther from the source, the wave speed of the shock decreases and approaches the ambient wave speed of the material. It is this ambient wave speed that the linear seismic wave propagation code uses as one of its material parameters.

Although some of the SESAME tables provide approximate ambient wave speeds, several do not and many that do contain warnings that the material models do not approach that provided wave speed in the ambient limit (Kerley and Christian-Frear, 1993). Because of this, we need to determine the appropriate ambient wave speed from the CTH tracer data itself. Travel times and true source-tracer distances ($\sqrt{r_{tr}^2 + z_{tr}^2}$) were computed for each pressure tracer. An example of an unprocessed CTH pressure tracer line along the z=0 axis (Figure 7) shows the moveout and change of shape of the pressure pulses as a function of distance. Travel times were automatically picked by finding the first time where amplitudes exceed 1% of the peak amplitude of the trace. A simple 1-D model of wave speed as a function of distance from the source was constructed by solving a linear inverse problem. Travel time (t_a) and wave speed (v)are related by

$$t_a = \int_0^d \frac{\mathrm{d}l}{v(l)} = \int_0^d s(l)\mathrm{d}l \tag{4.1}$$

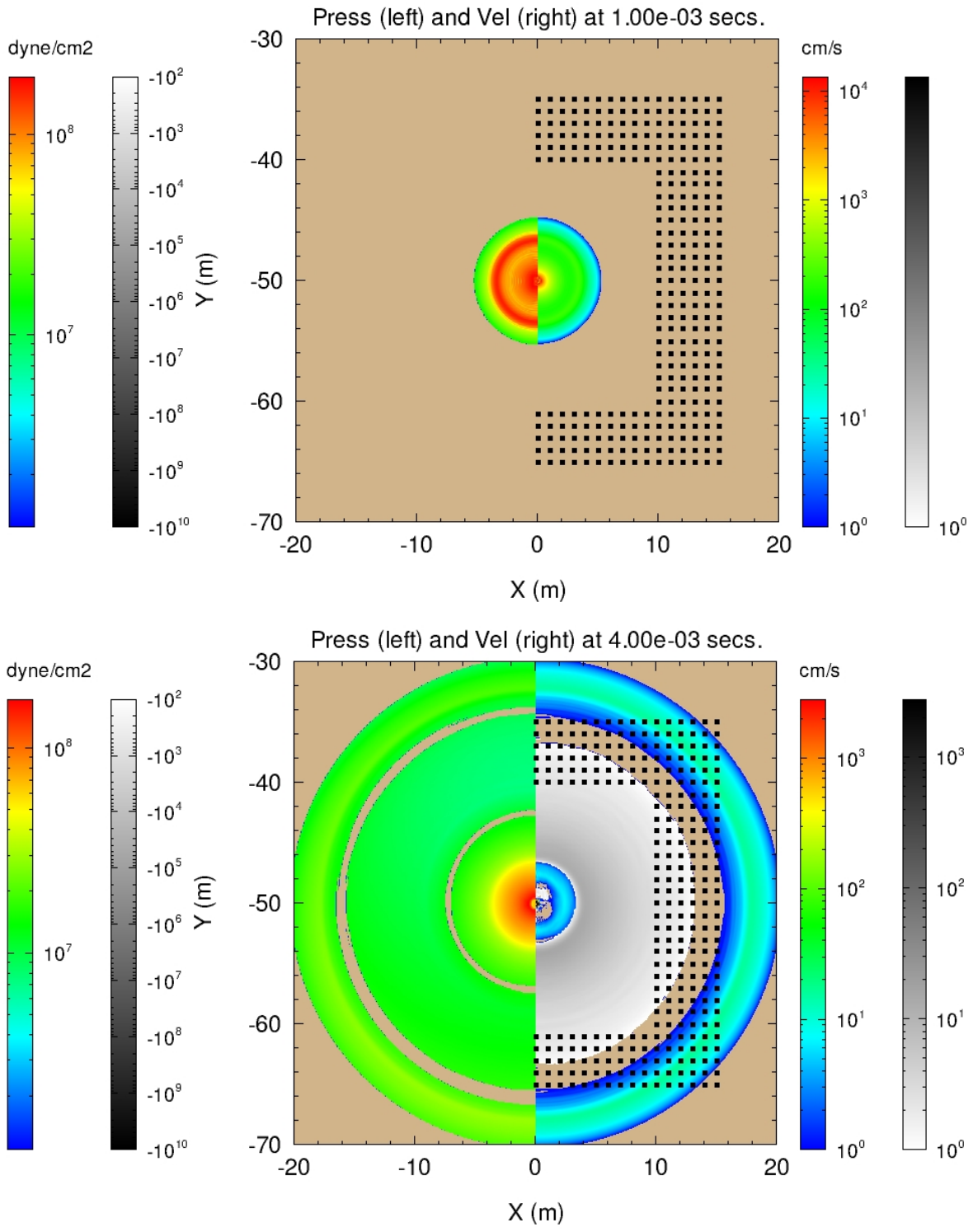

Figure 6: Outgoing shock wave at 1 ms (top) and 4 ms (bottom). The right half of each figure shows the magnitude of the radial velocity (outward motion colored; inward motion grayscale); the left half of each shows pressure (compression in color; tension in grayscale). Also shown are example tracer points (black squares). For illustrative purposes we do not show the full set.

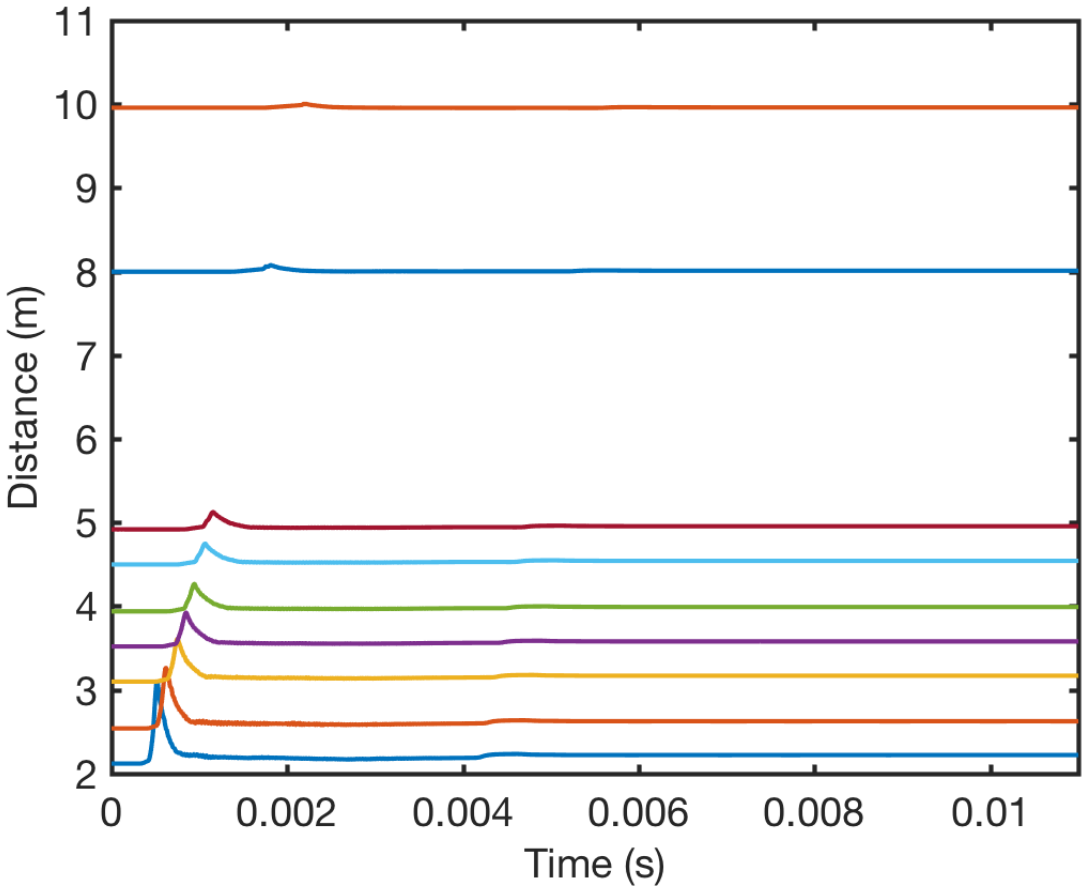

Figure 7: CTH pressure tracers along the z=0 axis from 2 m to 10 m from the source in quartz.

where s is the slowness (inverse of velocity). The rightmost equation in (4.1) is linear in slowness as long as the path traveled remains constant, which we are assuming in this simple analysis. This can be discretized into

$$t_a \approx \sum s_i \Delta l_i \tag{4.2}$$

where s_i is the slowness in cell i and Δl_i is the length of the cell. This can be reformulated into a linear system

$$\mathbf{As} = \mathbf{t_a} \tag{4.3}$$

where $\mathbf{A}$ is a matrix with number of rows equal to the number of tracers and number of columns equal to the number of cells. It contains entries equal to Δl_i at the appropriate locations. This would be sufficient with noise-free data, but numerical noise in the tracer output produced poor results when used alone. Thus, the system was regularized by imposing a smoothness constrain. The 1-D slowness model is constrained to be smooth in the Laplacian sense by augmenting the system of equations in (4.3) with

$$L_i = -s_{i-1} + 2s_i - s_{i+1} \tag{4.4}$$

for every cell i. The system of equations then becomes

$$\begin{bmatrix} \mathbf{A} \\ \mathbf{L} \end{bmatrix} \mathbf{s} = \begin{bmatrix} \mathbf{t_a} \\ \mathbf{0} \end{bmatrix} \tag{4.5}$$

where $\mathbf{L}$ contains the Laplacian smoothing coefficients. One can then solve for the slownesses in each cell. The results for each material is shown in Figure 8. Table 1 gives the ambient wave speed (Vp) determined for each material. The shear wave velocities (Vs) were computed by using the standard poisson ratio of 0.25 and densities were provided in the SESAME tables.

4.3. Elastic Radius and Effect of Coupling Distance

We desire to see how the distance at which the two codes are coupled affect waveforms and amplitudes. With our tracer geometry, we can choose where we couple CTH to the linear elastic code anywhere from 2 m to 15 m from the source. To see the effects on the far-field waveforms on our choice of the coupling distance, we

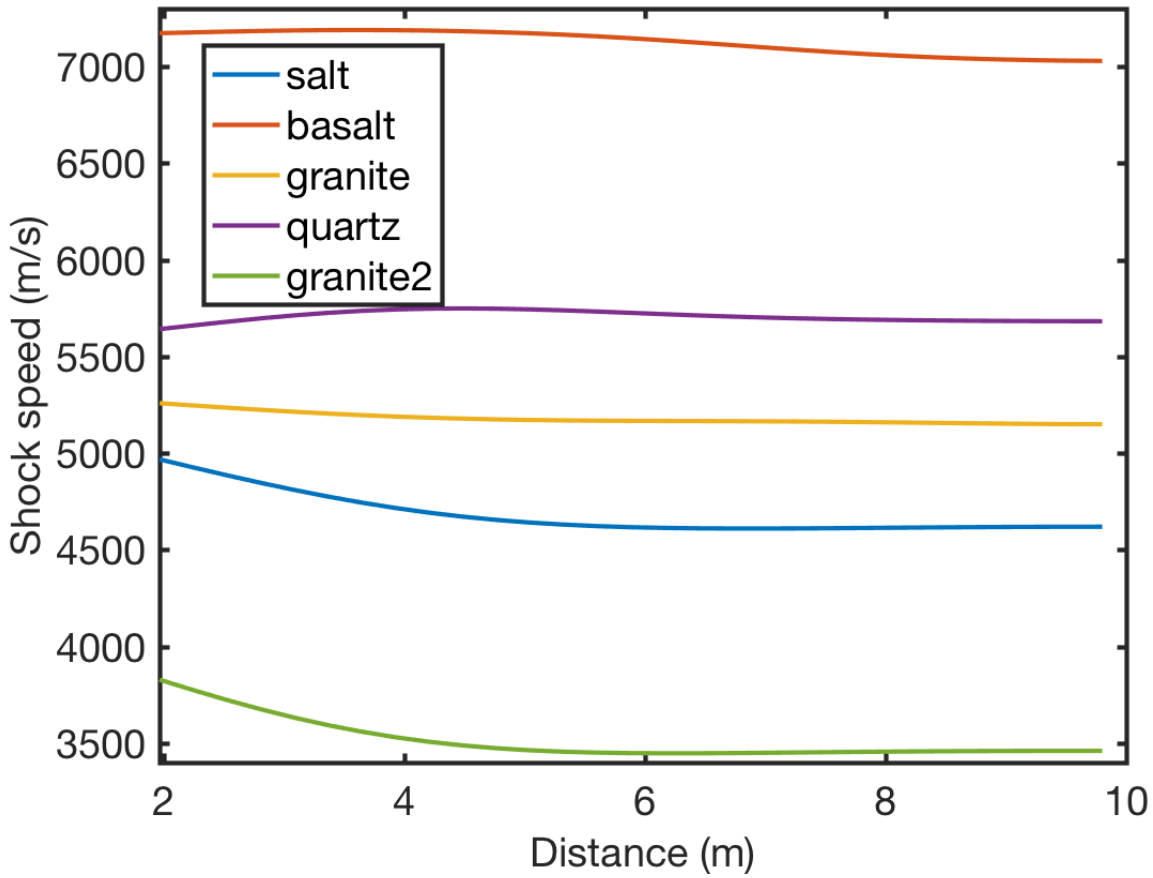

Figure 8: Computed shock wave propagation speed as a function of distance from the source in the five materials. Granite 2 is the weak granite model.

Table 1. Ambient Wave Speeds

Material	Vp (m/s)	Vs (m/s)	ρ (kg/m^3)
Salt	4620	2667	2145
Basalt	7030	4059	2868
Strong Granite	5150	2973	2551
Weak Granite	3450	1992	2551
Quartz	5683	3281	2205

try coupling distances of 2.1 m, 2.5 m, 3.1 m, 4.0 m, 4.5 m, 5.0 m, 6.0 m, 8.0 m, and 10.0 m from the source for all five materials. For quartz and the strong granite we also tried 12 m and 15 m. For weak granite, salt, and basalt the pressure waveforms are all shown at 10 m from the source, output from the linear elastic code, axiElasti after using time-varying boundary conditions at the locations given above (Figures 9-11). For quartz and strong granite we show the linear elastic pressure traces at 15 m (Figures 12-13). Legends in these figures are labeled according to coupling distances

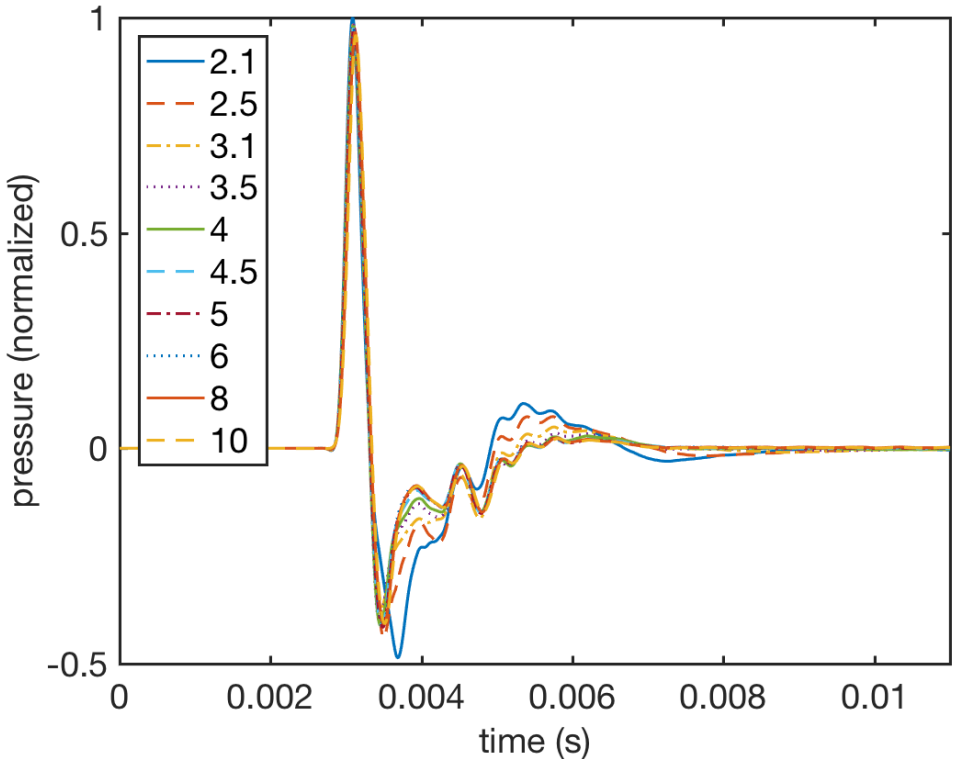

Figure 9: Effect of axiElasti pressure waveforms at 10 m using different coupling distances (legend) in the weak granite model.

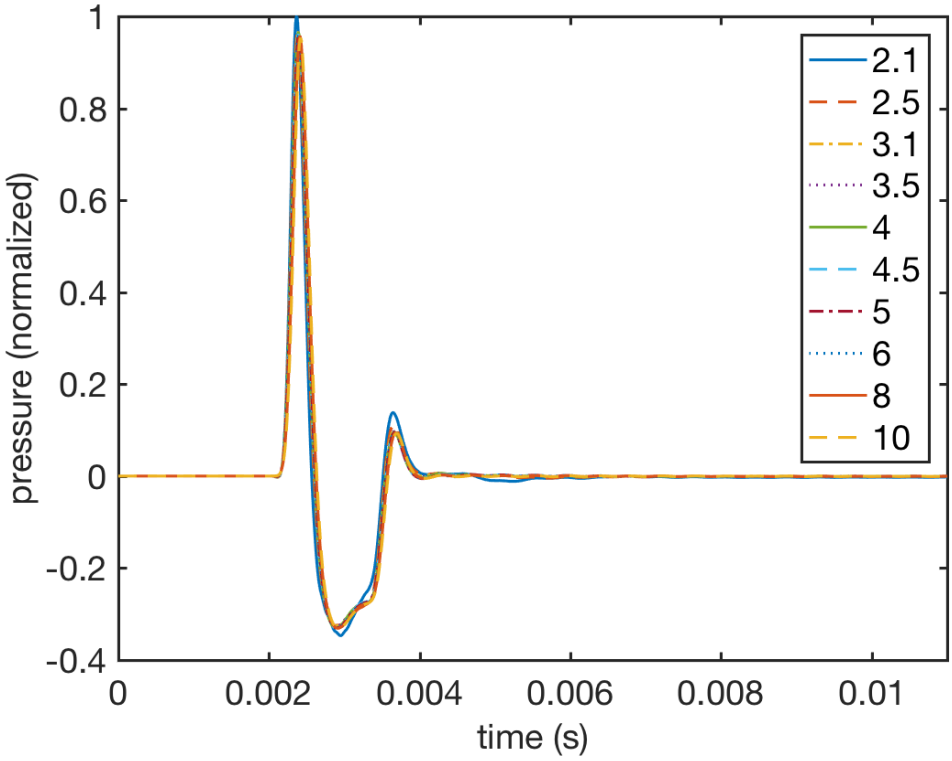

Figure 10: Effect of axiElasti pressure waveforms at 10 m using different coupling distances (legend) in the salt model.

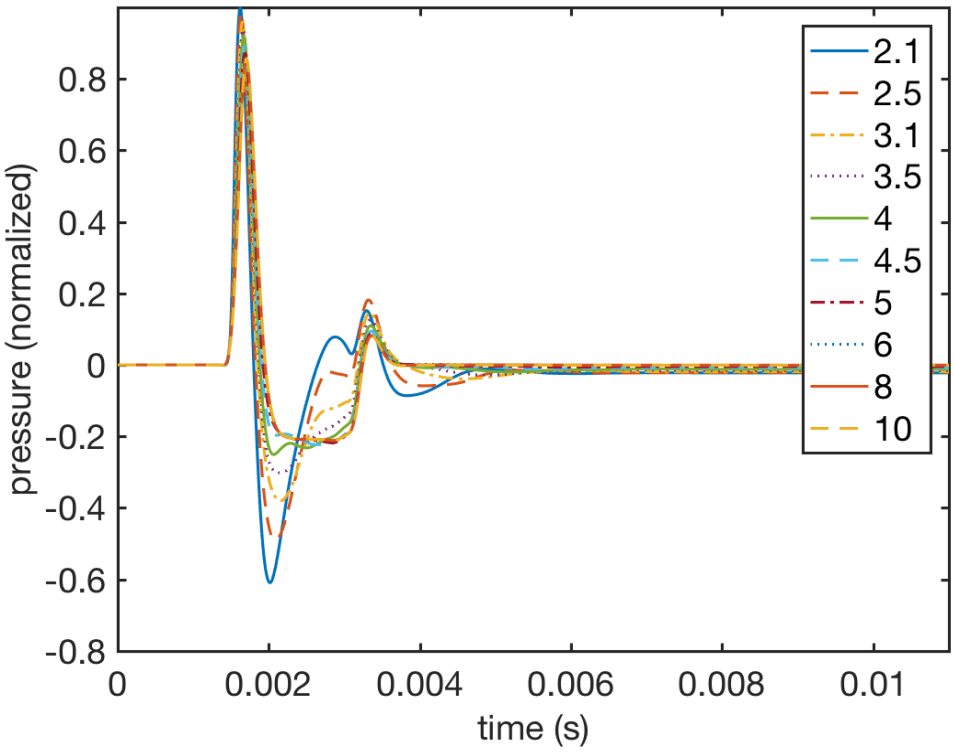

Figure 11: Effect of axiElasti pressure waveforms at 10 m using different coupling distances (legend) in the basalt model.

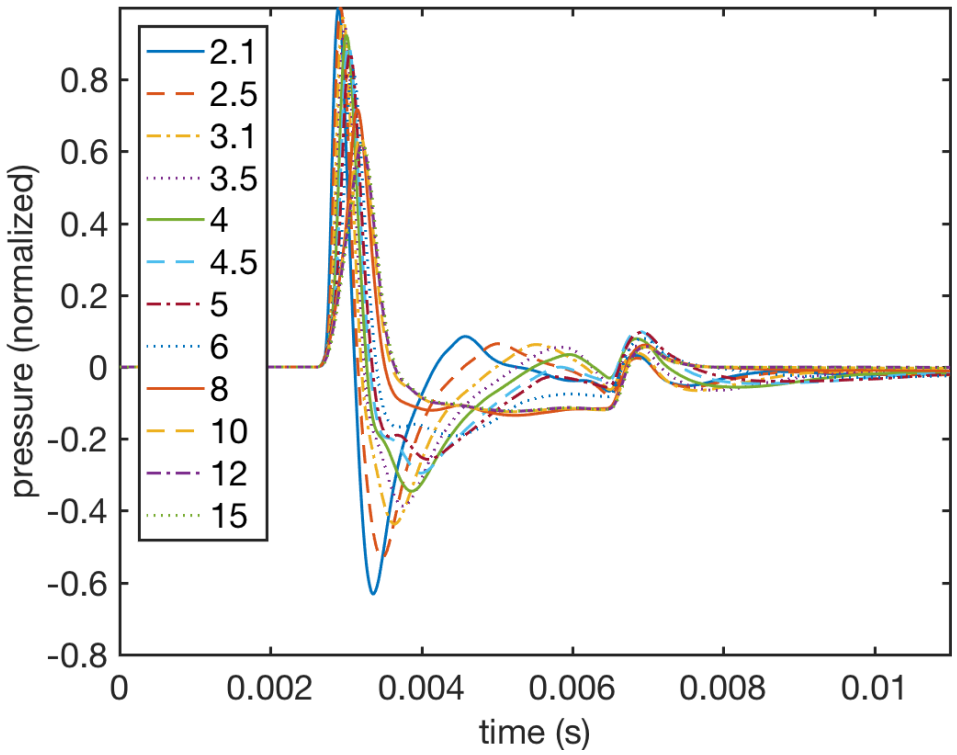

Figure 12: Effect of axiElasti pressure waveforms at 15 m using different coupling distances (legend) in the quartz model.

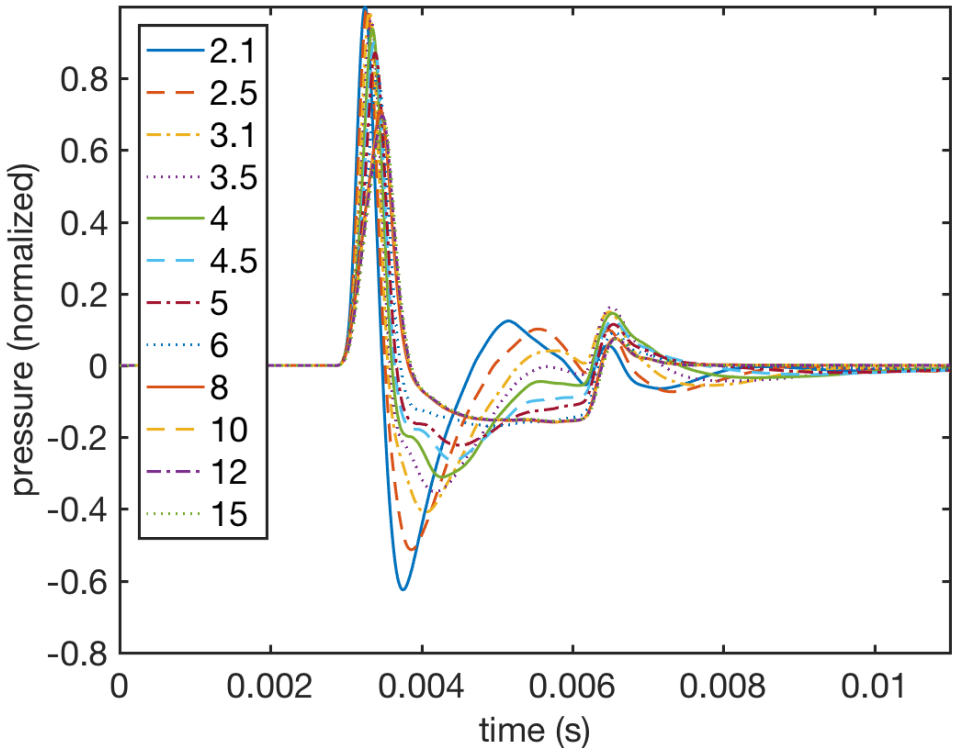

Figure 13: Effect of axiElasti pressure waveforms at 15 m using different coupling distances (legend) in the strong granite model.

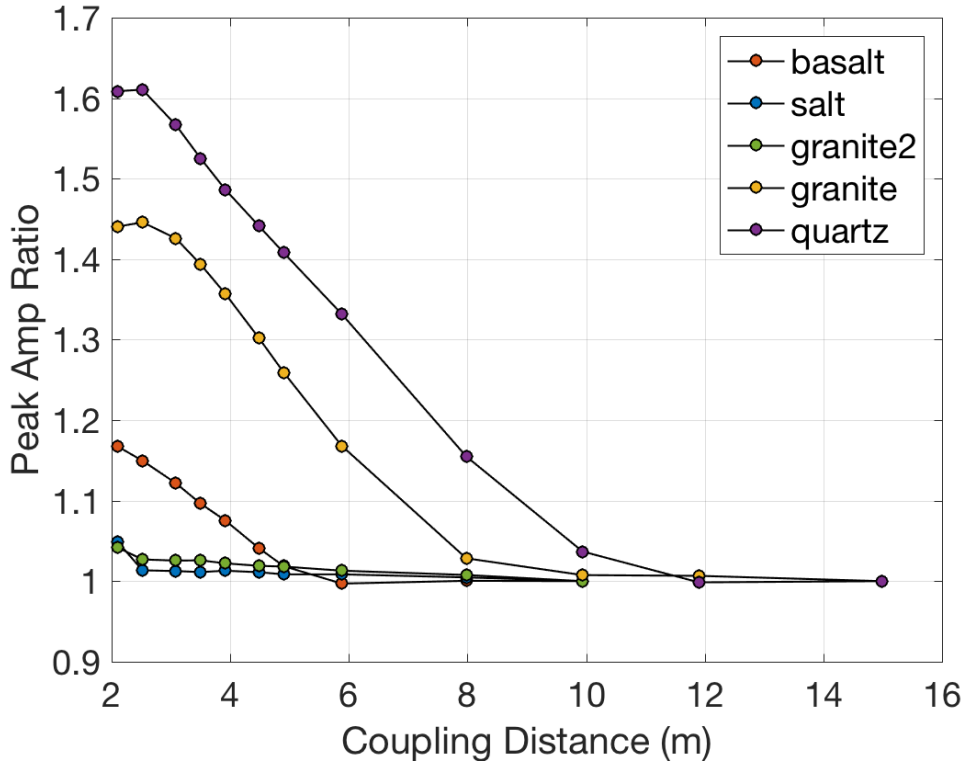

Figure 14: Peak amplitude ratios of axiElasti pressure waveforms as a function of coupling distance relative to farthest waveform.

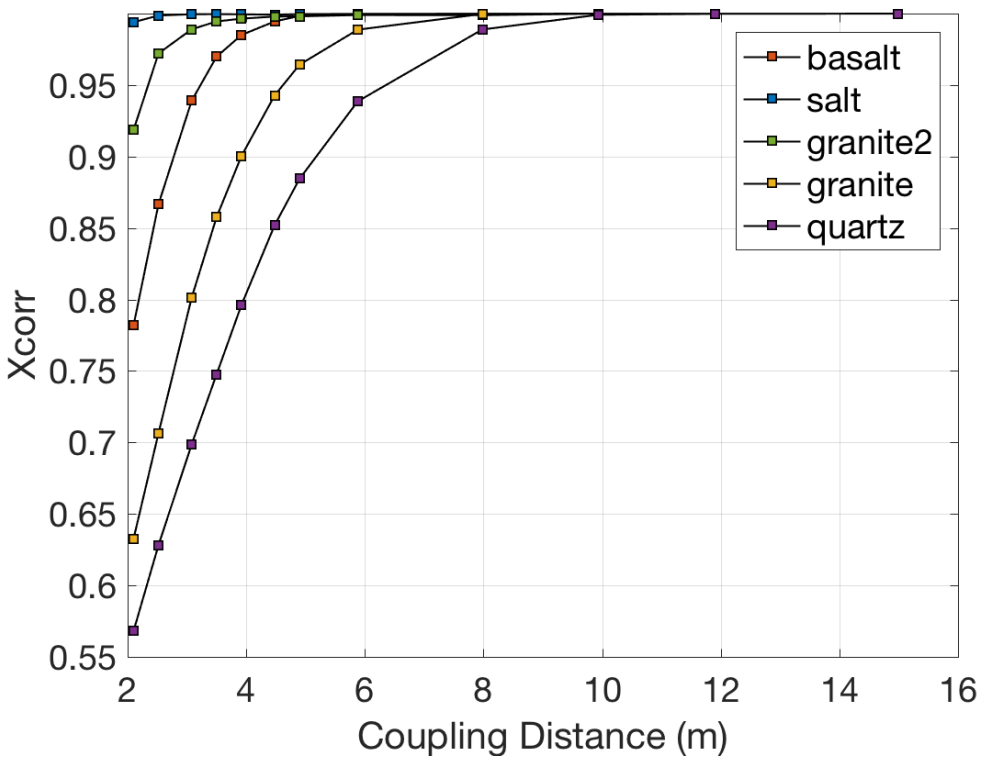

Figure 15: Cross-correlation coefficients of axiElasti pressure waveforms as a function of coupling distance relative to farthest waveform.

Table 2. Estimated elastic radii based on 1% error in peak amplitude and cross-correlation coefficient

Material	Peak Amp	Xcorr
Salt	5 m	2 m
Basalt	6 m	5 m
Strong Granite	10 m	8 m
Weak Granite	8 m	3.5 m
Quartz	12 m	10 m

(location of time-varying boundary condition interface). Output from the linear elastic code at farther observational distances shows similar behavior to those shown.

We would expect the far-field waveforms to remain constant if we choose a coupling distance beyond the elastic radius. Depending on the desired criteria, one can obtain different estimates of the elastic radius. We show the peak amplitude ratios of the waveforms and cross-correlation coefficients (Figures 14-15) versus coupling distances relative to the waveform from the farthest coupling distance. From this, if we choose 1% maximum error as the criteria, we obtain the estimates of the elastic radius given in Table 2 for both the case where the estimate is based on maximum amplitude or cross-correlation coefficient.

4.4. Discussion

The choice of the coupling distance does greatly affect the waveform shape and peak amplitudes of the far-field waveforms. As expected, once the wavefield is beyond the elastic radius, the far-field waveforms remain nearly constant. However, within the nonlinear region, the waveforms and amplitudes asymptotically approach the elastic region waveforms as distance increases. The elastic radius depends strongly on the material and also on the method used to compute the elastic radius. Waveform shapes approach the elastic waveforms at closer coupling distances than peak amplitudes. Weaker materials (weak granite and salt) have a greater difference in elastic radii computed via peak amplitude and cross-correlation.

The observation that the waveform shape approaches the linear waveform shape at closer distances than amplitudes suggests that one could couple the codes at the elastic radius determined by cross-correlation and then appropriately scale the waveforms to correct for the amplitude mismatch. This approach could save significant computational effort in certain simulation scenarios since CTH calculations require substantially more computational resources than linear elastic wave propagation codes. This would be especially relevant for 3-D scenarios where the difference in computational cost between the algorithms is even greater. However, this will require further research into what the appropriate amplitude scaling constant is for different models and simulation scenarios. For example, these simulations were computed for a

10 kg TNT explosion; however, does the scaling constant depend on yield? There may be other factors that need investigated to determine how they many affect the scaling constants.

Figures 9-13 demonstrate the strong effect of nonlinearities on the waveform shape and how that shape evolves as the shock wave propagates. Further research is needed to understand how the source itself (e.g., yield), heterogeneity near the source, and 3-D effects, among others, effect the evolution of the waveforms toward those that propagate to the far-field where seismic receivers are typically located.

5. CONCLUSIONS AND FUTURE WORK

In this report we have described the development of a 2-D axisymmetric, cylindrical coordinate system algorithm for simulation of linear elastic wave propagation called axiElasti. This algorithm has the additional ability to couple to the nonlinear, shock propagation code CTH through time-varying boundary conditions. This allows end-to-end simulation of an explosion, for example, accounting for the complex nonlinear effects near the source while then switching to a more computationally efficient and accurate linear wave propagation solver in the far-field, linear regime. One obtains the benefits of both algorithm types within the respective regimes for which they were designed, enabling a more complete understanding of the physical processes that affect the evolution of the wavefield from the near-field to far-field.

One important factor in how the wavefield evolves is the elastic radius. In this report we performed numerical experiments with simple homogenous earth materials using the code coupling developed as part of this project. We investigated the location of the elastic radius and how choice of the coupling location between the two algorithms affects waveforms observed in the far-field. The location of the elastic radius is strongly dependent on the material type. It also depends on how one defines it. We tested two methods of determining the elastic radius: peak amplitude ratios and cross-correlation coefficient relative to a far-field waveform as a function of code coupling distance. For all materials tested, the cross-correlation coefficient estimates a smaller elastic radius compared to radii based on peak amplitude ratios, indicating that waveform shape more rapidly approaches the linear one with distance compared to amplitude. Secondly, weaker materials have a greater difference in elastic radii computed with the two methods.

This report barely scratches the surface on the utility of coupled codes and there remain many questions that can be addressed with these algorithms. For example, we noticed that waveform shape approaches the linear regime waveforms quicker than amplitude. This suggests computational resources could be saved provided the correct scaling factor could be applied. However, what factors influence this scaling relationship and when can or cannot it be used? In addition to this specific question, more general questions remain, such as how the source itself, local earth structure, 3-D effects, topography, etc., influence the evolution of the wavefield from the extreme near-field to typical seismological observation distances in the far-field. These and many other questions can be addressed with this code. Future plans include extending the code coupling principles outlined in this report to the existing 3-D linear elastic wave propagation code, Parelasti. This enhancement will enable more complex and geologically realistic simulations and investigations with end-to-end modeling.

REFERENCES

1. Aldridge, D.F. and M.M. Haney, *Numerical dispersion for the conventional-staggered-grid finite-difference elastic wave propagation algorithm*, SAND2008-4991, Sandia National Laboratories, Albuquerque, NM, July 2008.

2. Collino, F. and P.B. Monk, Optimizing the perfectly matched layer, *Comput. Methods Appl. Mech. Engrg.*, 164, 157-171, 1998.

3. Dahlen, F.A. and J. Tromp, *Theoretical Global Seismology*, Princeton University Press, Princeton, NJ, 1998.

4. Kerley, G.I. andT.L. Christian-Frear, *Sandia equation of state data base:* seslan *file*, SAND93-1206, Sandia National Laboratories, Albuquerque, NM, June 1993.

5. Komatitsch, D., and R. Martin, An Unsplit Convolutional Perfectly Matched Layer Improved at Grazing Incidence for the Seismic Wave Equation, *Geophys.*, 72 (5), SM155-SM167, doi 10.1190/1.2757586, 2007.

6. Marsden, J.E. and A.J. Tromba, *Vector Calculus*, W.H. Freeman and Company, New York, NY, 1988.

7. Moczo, P., J. Kristek, V. Vavrycuk, R.J. Archuleta, and L. Halada., 3D heterogeneous staggered-grid finite-difference modeling of seismic motion with volume harmonic and arithmetic averaging of elastic moduli and densities: *Bull. Seis. Soc. of Am.*, 92, 3042-3066, 2002.

8. Preston, L.A., D.F. Aldridge, N.P. Symons, Finite-Difference Modeling of 3D Seismic Wave Propagation in High-Contrast Media, *Soc. Expl. Geophys. 2008 Annual Meeting Extended Abstracts*, 2008.

9. Schmitt, G., A.L. Brundage, D.A. Crawford, E.N. Harstad, K. Ruggirello, S.C. Schumacher and J.S. Simmons, *CTH User's Manual and Input Instructions, Version 11.2, CTH Development Project*, Sandia National Laboratories, Albuquerque NM, 2016.

10. Snelson, C.M., R.E. Abbott, S.T. Broome, R.J. Mellors, H.J. Patton, A.J. Sussman, M.J. Townsend, and W.R. Walter, Chemical Explosion Experiments to Improve Nuclear Test Monitoring, *EOS Trans.*, 94 (27), 237-239, 2013.

DISTRIBUTION

1	MS0406	William Hilbun	6756 (electronic copy)
1	MS0750	Hunter Knox	8861 (electronic copy)
1	MS0899	Technical Library	9536 (electronic copy)


Sandia National Laboratories